Chapter 4

Predicting and inverting migration velocities

4.1 INTRODUCTION

In the preceding chapter I described how to find a linear operator relating perturbations in interval slownesses to the resulting perturbations in prestack time-migration velocities. Migration velocities can be measured from data using the methods of the chapter 2. The desired goal is then to invert the linear operator of chapter 3, solving for interval velocities by using the observed migration velocities as data. However, such an inversion can be no better than one's knowledge of the artifacts, errors, and limitations of the method; it is easier to set up "black box" inversion schemes than to know how much to trust the purported answers they provide. Thus, I devote most of this chapter to synthetic modeling, using the linear operator to predict migration velocities from interval velocities, and to inversion, using singular value decomposition of the operator to analyze the resolution limits and to illustrate the expected artifacts. To analyze field data, one must go beyond the linear inversion to nonlinear inversion, using the linear operator to define a gradient direction for iteratively improving an initial model. In section 4.5 I discuss how to formulate such a nonlinear inversion algorithm.

4.2 PREDICTING THE EFFECTS OF SLOWNESS ANOMALIES

The operator $\mathbf{G}_s$ derived in chapter 3 predicts changes in migration slowness for specified perturbations in interval slowness. How good are these predictions? To test this, I created simple structural models, introduced slowness anomalies, and generated synthetic data using finite-difference modeling. I then created migrated images using the velocity-space DMO and migration algorithm of chapter 2, and measured the slownesses at which the images had maximum energy. These results can then be compared with the slownesses predicted using the $\mathbf{G}_s$ operator applied to the model slowness perturbations.

Flat bed example

Figure 4.1 shows a slowness model containing a flat bed, and above it, a circular anomaly in the background slowness. The slowness in the upper layer is 0.5 s/km, and that in the lower layer is 0.33 km/s. The slowness anomaly has a peak value of 0.476 s/km at the center, and decays as a Gaussian function to the background of 0.5 s/km. This anomaly is chosen to be very smooth, so that it affects only transmitted waves; reflections from the anomaly are extremely weak. The zero-offset synthetic data from the finite-difference modeling are shown in Figure 4.2. A cable length of 1 km is used in the modeling; the model is 4 km long, and the reflecting bed is at a depth of 2 km.

The migration slownesses measured along the flat reflecting bed are shown as stars in Figure 4.3; because the bed is flat, the migration slownesses are equal to stacking slownesses. The slownesses predicted using the operator of chapter 3 are overlaid as a solid curve for comparison. The predicted values fit the data well, displaying the same shape and amplitude. Small differences are expected for several reasons. First, I have used a linear approximation to a nonlinear relation. Second, least-squares fitting of traveltimes is not identical to stacking of waveforms. Third, there are errors inevitably made in picking peaks from the velocity analysis. The first two reasons probably account for the difference seen here in the peak amplitudes between the predicted and measured values. For application to field data, the picking errors can in practice probably often override other considerations.

I have stated before that, for flat beds, the difference between the operator I use and that used by Toldi (1985) is minor. The curve predicted using Toldi's operator is indistinguishable from that in Figure 4.3 (on the scale of this plot), confirming that the choice of weighting function has only a minor effect on the operator.

Dipping bed example

Figure 4.4 shows a slowness model containing a bed with 20° dip, and above it, a circular anomaly in the background slowness. Like the flat bed model in Figure 4.1, the slowness in the upper layer is 0.5 s/km, and that in the lower layer is 0.33 km/s. The slowness anomaly is identical to the one in figure 4.1, as are cable and model dimensions. The zero-offset synthetic data from finite-difference modeling is shown in Figure 4.5. Figure 4.6 shows the stacking slownesses measured from the data; the expected pattern of a positive central peak flanked by regions of negative response is again observed. Figure 4.7 shows the response predicted for migration slownesses using the $\mathbf{G}_s$ operator from chapter 3. Figure 4.8 shows the migration

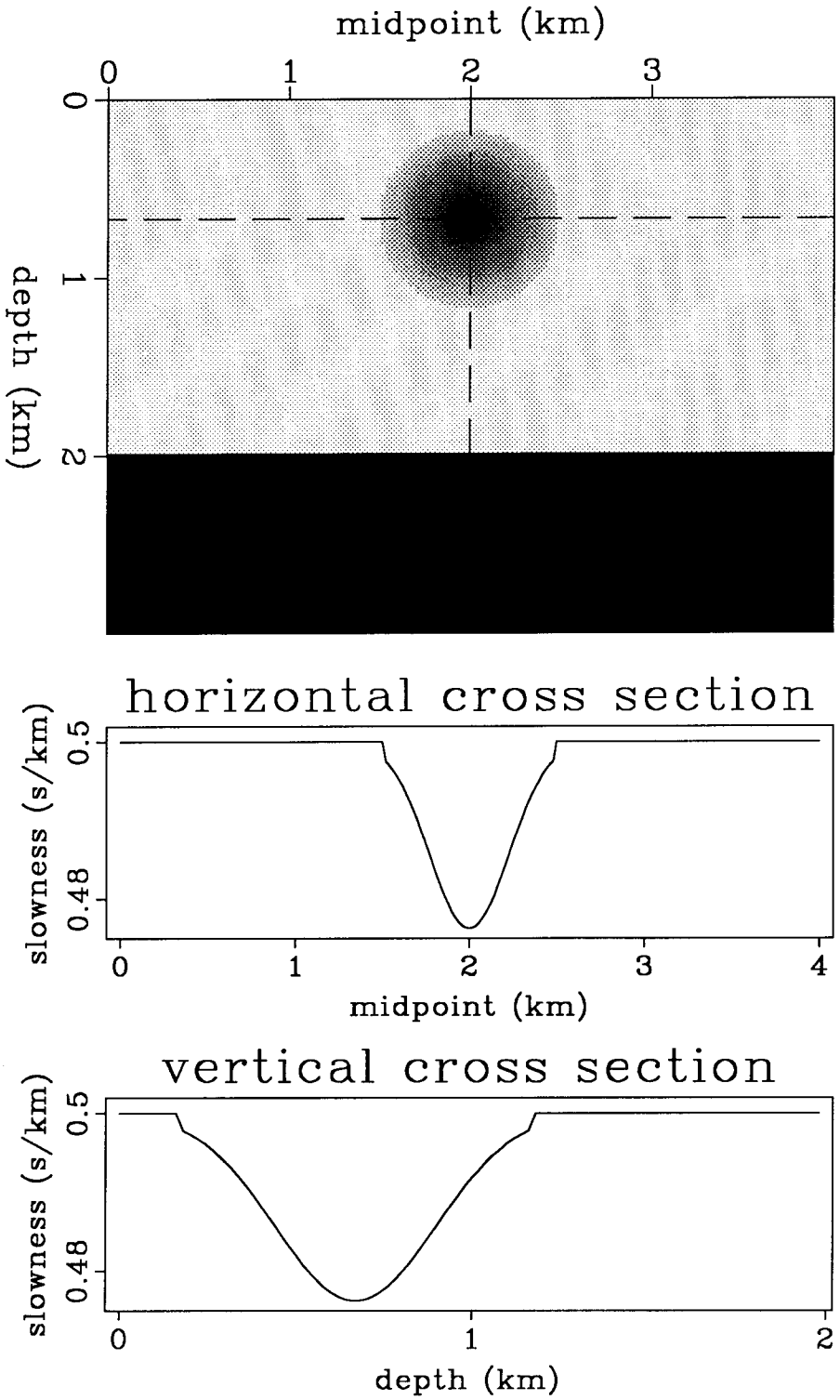

FIG. 4.1. Slowness model with a flat reflector and a Gaussian anomaly. Slowness in the upper layer is 0.5 s/km, and in the lower layer is 0.33 s/km. The peak of the circular anomaly has a slowness of 0.476 s/km. The lower figures show horizontal and vertical cross sections through the anomaly along the dashed lines in the upper figure. This model is used to generate the data in Figure 4.2.

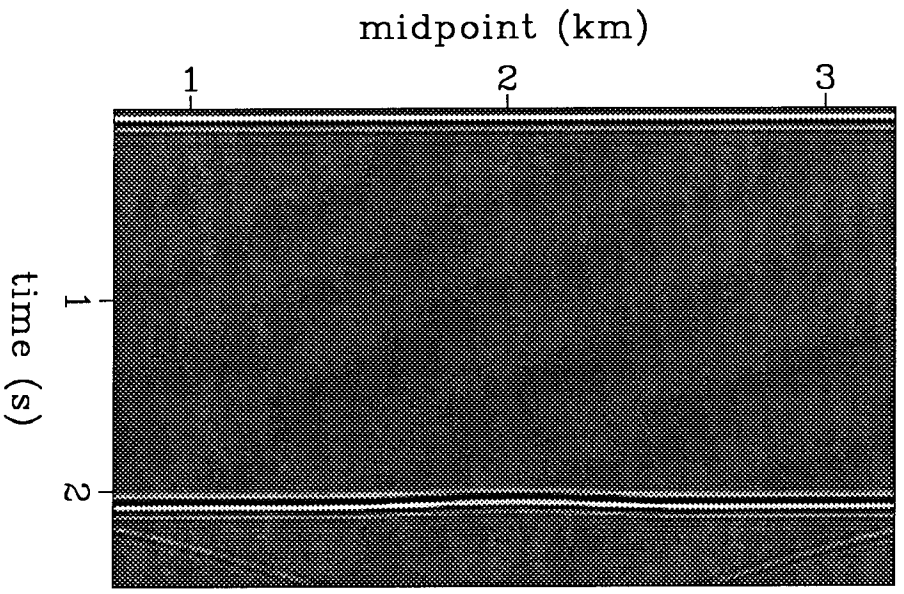

FIG. 4.2. Synthetic zero offset section generated by finite-difference modeling using the slowness model in Figure 4.1. The effect of the slowness anomaly is visible as a pullup on the flat reflector. Weak reflections below the reflector are artifacts from reflections off the edges of the model.

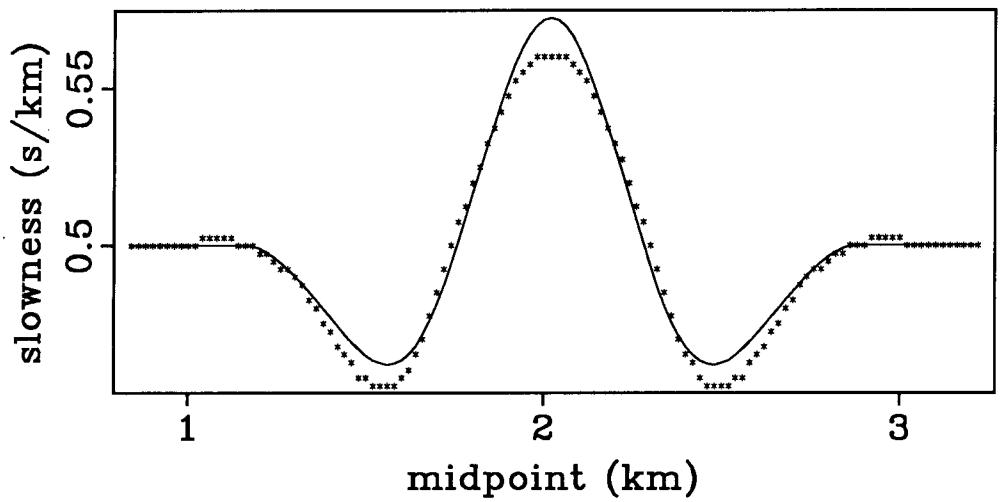

FIG. 4.3. Migration (stacking) slownesses for the flat bed in Figure 4.1. The solid curve is predicted using the $\mathbf{G}_s$ operator described in this paper. The stars are values measured from processing finite-difference synthetic data.

slownesses measured from the data by an automatic peak-picking program. Figure 4.8 is extremely noisy and is dominated by a strong left-to right trend from high slowness to low; although an anomalous response can be seen in the middle of the figure, on the whole it shows little resemblance to the prediction in Figure 4.7. What has gone wrong?

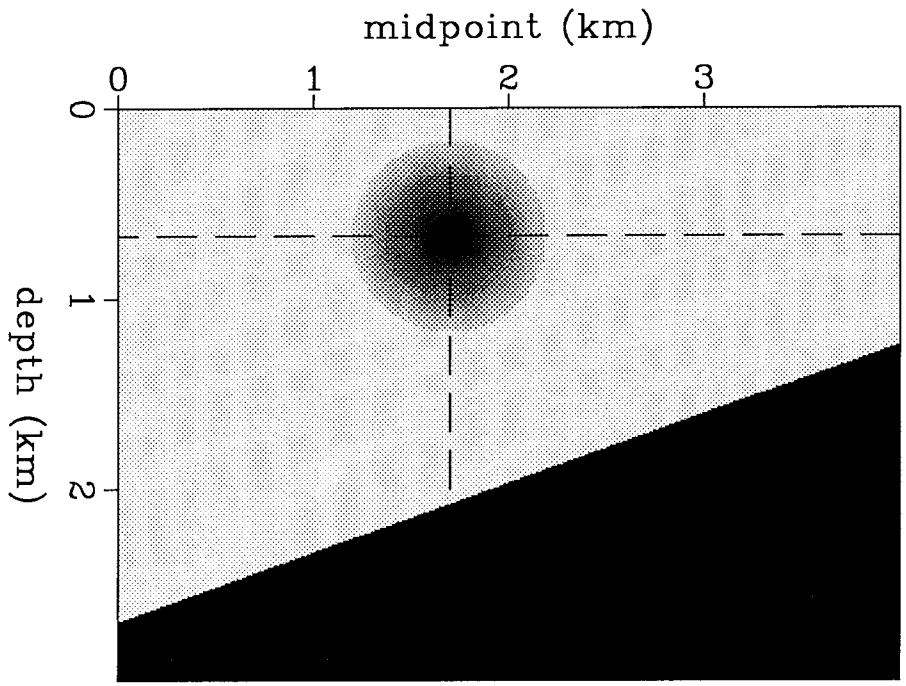

FIG. 4.4. Slowness model with a dipping reflector and a Gaussian anomaly. Slowness in the upper layer is 0.5 s/km, and in the lower layer is 0.33 s/km. The peak of the circular anomaly has a slowness of 0.476 s/km; it decays the same as the anomaly in Figure 4.1. This model is used to generate the data in Figure 4.5.

Figures 4.7 and 4.8 actually should not be compared to each other directly. The predicted curve in Figure 4.7 shows the migration slowness as a function of lateral location on the dipping reflector. Figure 4.8 shows the measured migration slowness as a function of migrated midpoint. However, the mapping between a physical reflection point on the bed and its location after migration depends on the migration slowness, so at each migrated midpoint one is seeing not a single fixed reflection point, but the images of many different points, depending on the migration slowness used. This can be seen in Figure 4.9, which shows a contour plot of the peak energy

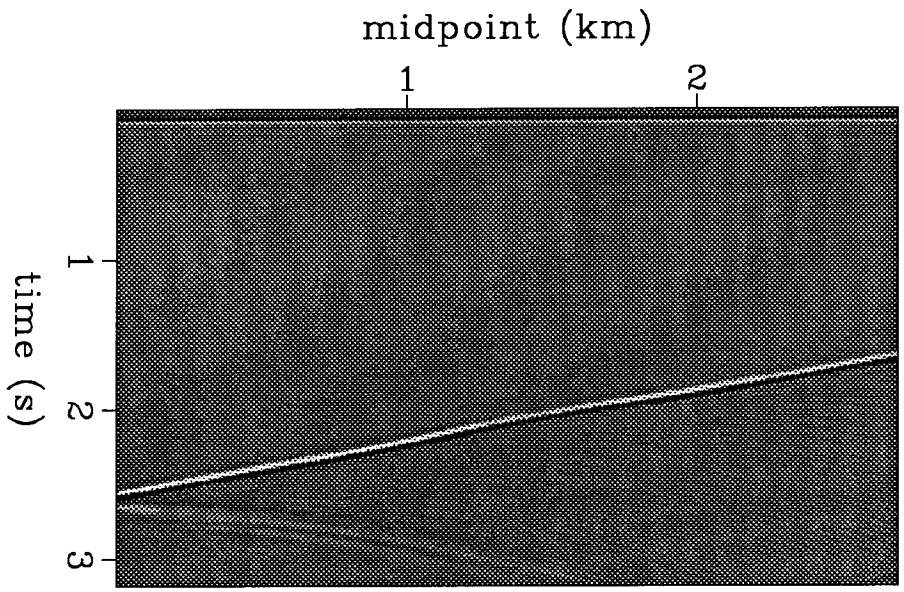

FIG. 4.5. Synthetic zero offset section generated by finite-difference modeling using the slowness model in Figure 4.4.

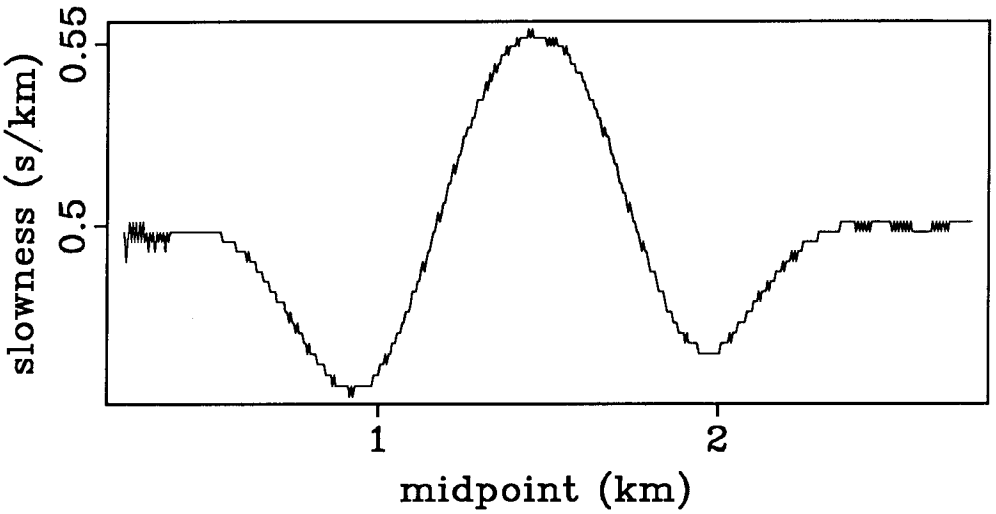

FIG. 4.6. Stacking slownesses measured for the dipping bed in Figure 4.4. These values are derived from processing finite difference data.

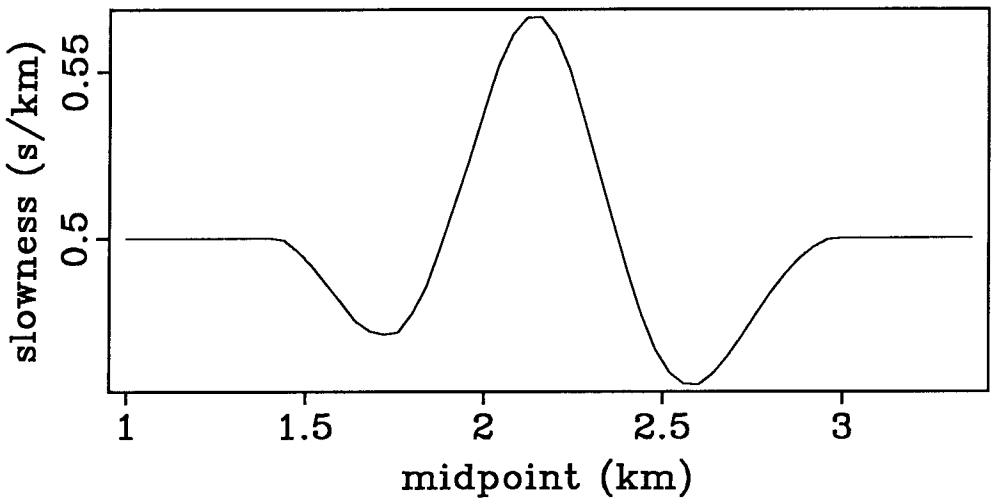

FIG. 4.7. Migration slownesses predicted for the dipping bed in Figure 4.4, using the $\mathbf{G}_s$ operator of chapter 3.

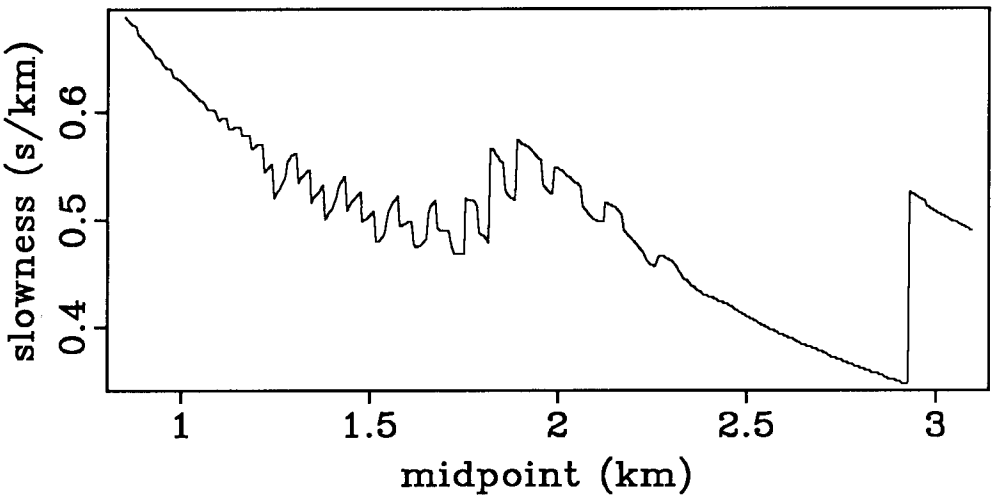

FIG. 4.8. Migration slownesses measured for the dipping bed in Figure 4.4. These values are derived from processing finite difference data.

as a function of both migrated midpoint and slowness; this type of display is called a horizon velocity (or slowness) analysis. Contours of peak energy can be seen to skew severely as slowness increases. In other words, as migration slowness decreases, a given event moves updip, so a velocity analysis at a constant migrated midpoint is

not the same as one at a constant reflection point. (The amount that events move as migration slowness changes is calculated in Appendix F.) A velocity analysis that attempts to maximize the total energy will try to pick a single dominant high amplitude event at many migrated midpoints; this is the source of the strong trend in Figure 4.8. Careful amplitude balancing might lessen this problem. In this sense, the single-bed finite-difference synthetic used here is more difficult to analyze than field data might prove to be, because there are no other reflectors present here to provide constraining velocity information, and because amplitude balancing methods such as AGC (see section 2.5) unacceptably magnify modeling artifacts arising from boundary reflections and numerical wavelet dispersion.

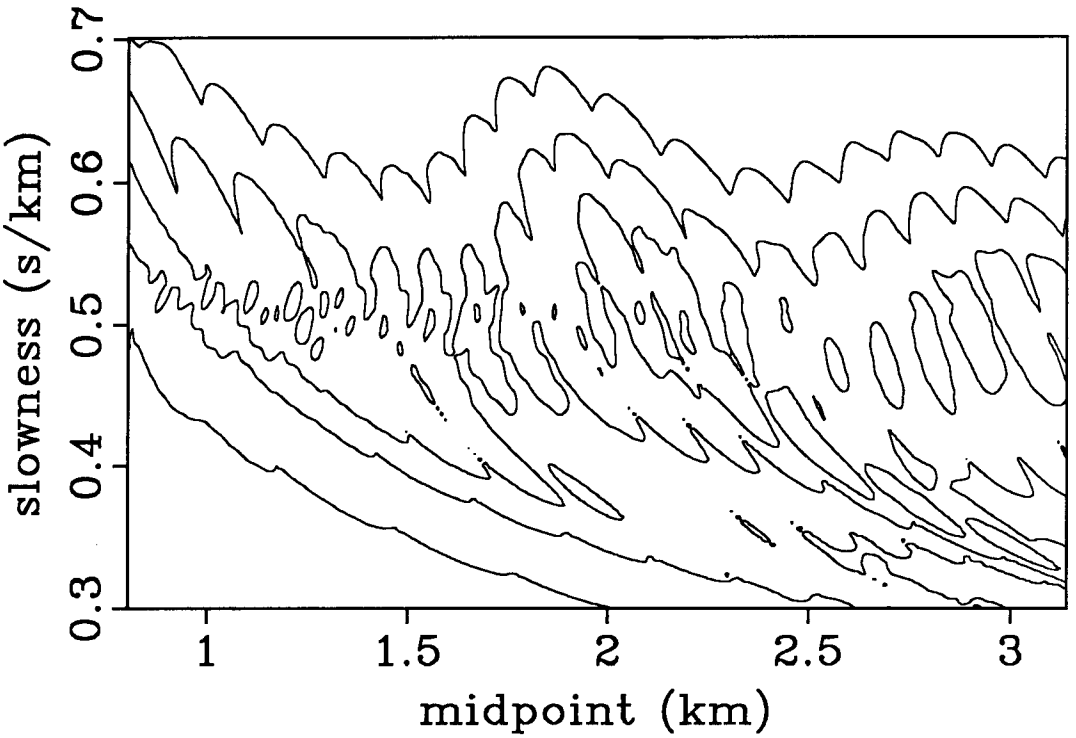

FIG. 4.9. Horizon slowness analysis for the dipping bed in Figure 4.4. This figure shows contours of peak energy as a function of migrated midpoint and migration slowness.

The effect of the movement of events as migration slowness changes is to skew the predicted curve in Figure 4.7. Applying a mapping compensating for this skewing to Figure 4.7 converts the axis from reflector point location to migrated midpoint, yielding the curve shown in Figure 4.10. This curve is closer to the shape of the anomaly seen in the middle of Figure 4.8, but noise and the strong left-to-right trend still dominate that figure.

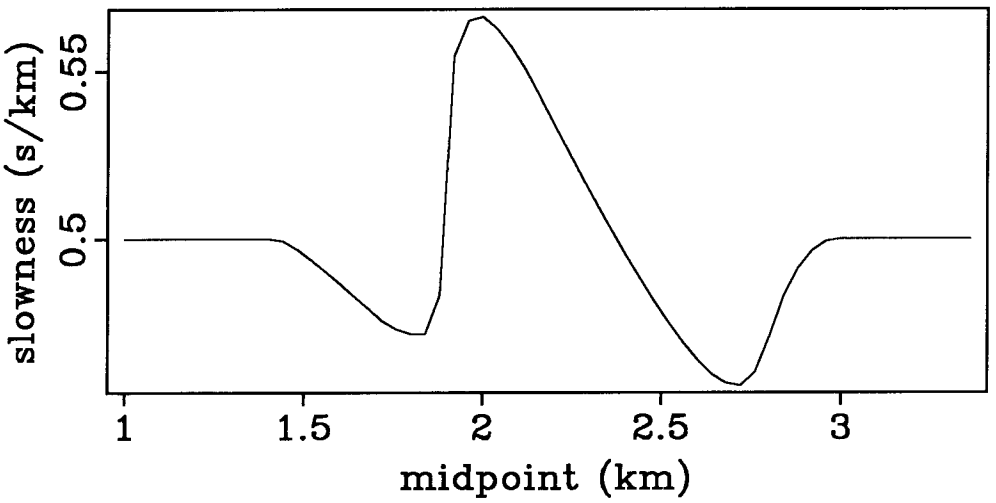

FIG. 4.10. Predicted migration slowness as a function of migrated midpoint. Note that this figure differs from Figure 4.7, which shows migration slowness as a function of physical location on the dipping bed.

To attack the skewing problem effectively, one needs to compare energy values for the different data points that correspond to a fixed subsurface reflector point. Directly tracking events on a bed is difficult, because one has to allow precisely for the traveltime pullup as slowness changes, and also for the lag between onset and peak of the wavelet. Another way to compensate for the difference between subsurface reflector position and migrated midpoint is to correct the horizon velocity analysis for the skewing effect, as shown in Figure 4.11. In this figure, I have also low-pass filtered and amplitude balanced the data over midpoint. The predicted migration slowness anomaly pattern from Figure 4.7 is superposed on the energy contours in Figure 4.11 as a heavy dashed line. The contours of greatest energy now do show the expected anomaly pattern, but they still only approximately match the predicted curve.

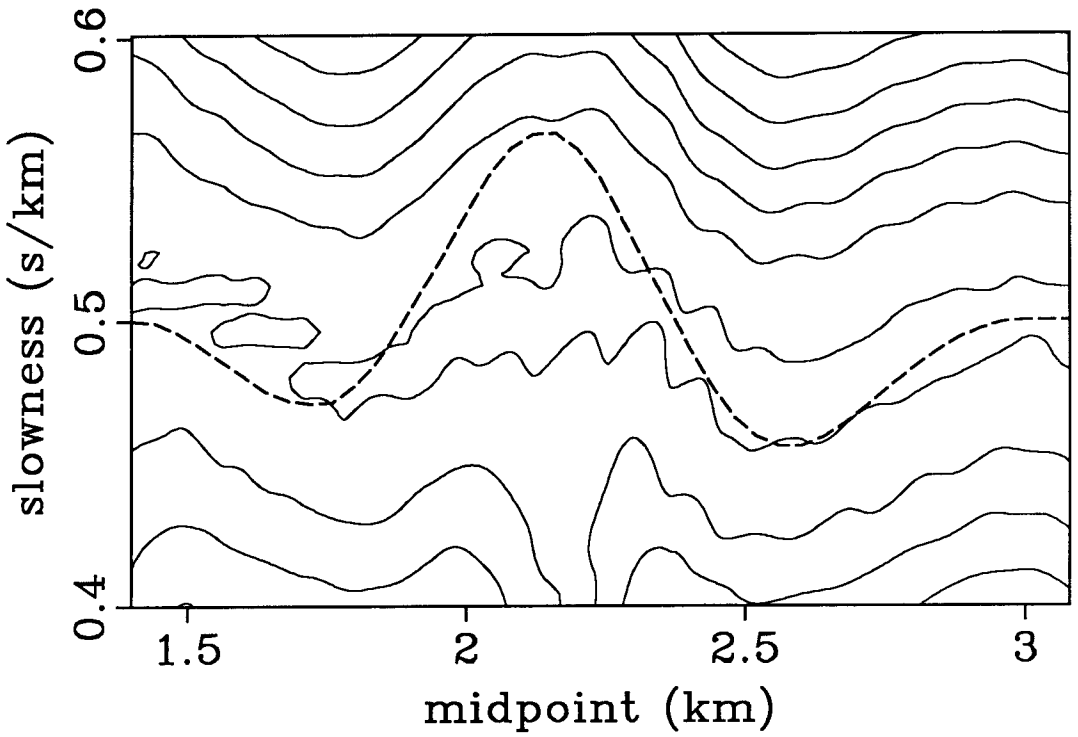

FIG. 4.11. Horizon slowness analysis for the dipping bed in Figure 4.4. This figure shows contours of peak energy as a function of migrated midpoint and migration slowness. The figure is low pass filtered and balanced over midpoint, and is kinematically compensated for the skewing introduced by the movement of events caused by migration at different slownesses. The dashed line shows the predicted migration slownesses from Figure 4.7.

The compensation for skewing used in Figure 4.11 is, in effect, a kinematic residual migration that attempts to convert the positions of events to where they would be if they were all migrated at the background slowness of 0.5 s/km. This compensation could also be done by applying a wave-theoretical residual migration (Rothman et al., 1985) to each migrated section. Equivalently, one can migrate each panel using not the various DMO-corrected stacking slowness, but instead using the same background slowness for all panels. A horizon velocity analysis generated from data processed this way is shown in Figure 4.12. No skewing or smoothing is applied this time. The expected anomaly pattern is clearly outlined by the energy contours. Figure 4.13 shows the picked energy peaks compared with the predicted anomaly curve from Figure 4.7. The measured curve is still somewhat noisy, but the agreement with the prediction is much improved.

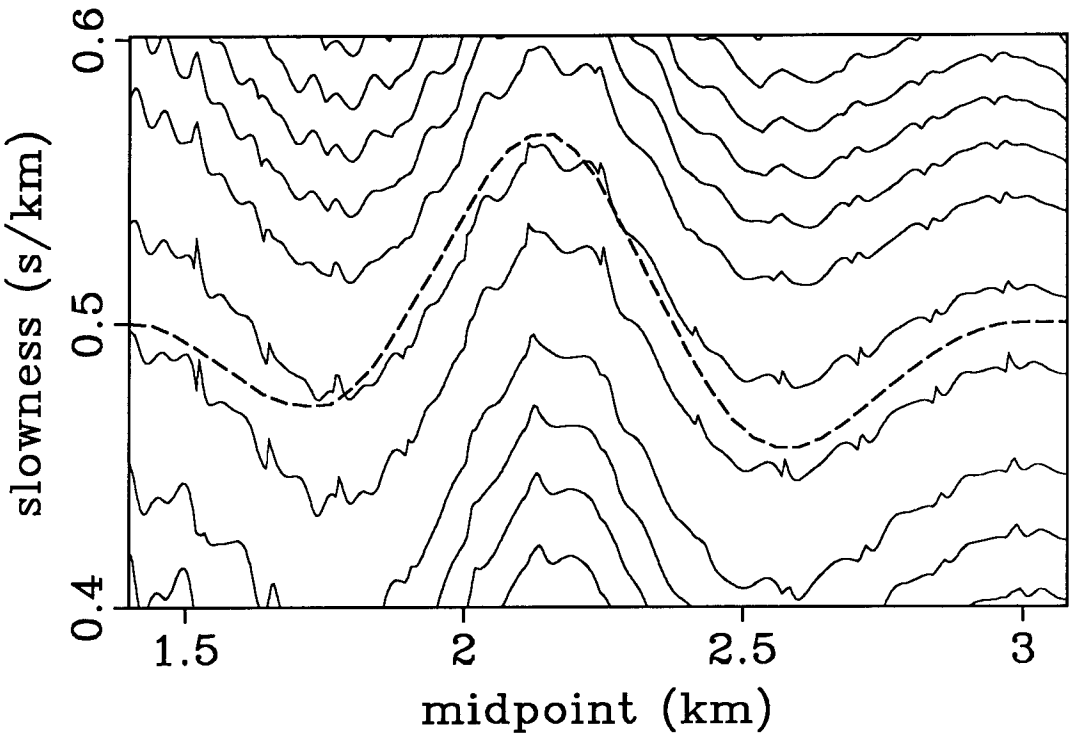

FIG. 4.12. Horizon slowness analysis for the dipping bed in Figure 4.4. This figure shows contours of peak energy as a function of migrated midpoint and migration slowness. This figure is generated using data that are all migrated with the same background slowness, rather than with a different slowness for each stacked section. The dashed line shows the predicted migration slownesses from Figure 4.7.

Thus, for this example, migrating DMO-corrected sections with a single background slowness produces a substantially better velocity analysis than migrating each section with its respective DMO-corrected stacking slowness. The velocity information used in maximizing an energy measure is calculated from the comparing the different data at different offsets; the movement in midpoint during zero-offset migration does not change the total energy in a section, and, for the synthetic example analyzed here, actually makes it more difficult to measure the energy peaks reliably, rather than helping. Moreover, if the background slowness is not everywhere constant, migrating all the sections with a variable velocity field adds considerably to the computational cost. It is thus attractive to consider leaving out the zero-offset migration entirely, and to examine instead slowness analysis based on the unmigrated, but DMO-corrected, sections. As discussed in section 3.10, the slownesses measured from DMO-corrected but unmigrated data are essentially the same as those from a migration analysis, but with the values assigned to unmigrated, rather than

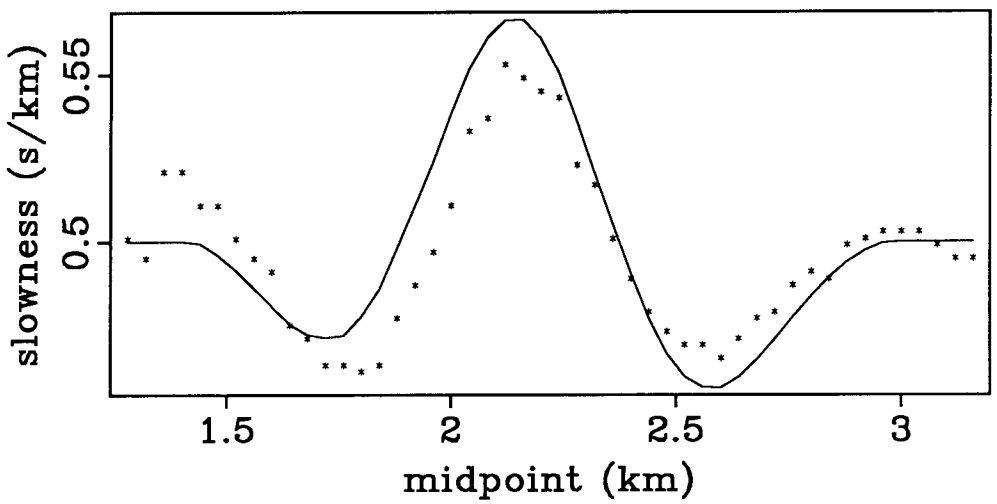

FIG. 4.13. Migration slownesses for the dipping bed in Figure 4.4. The solid curve shows the predicted migration slownesses from Figure 4.7. The stars are peak values picked from Figure 4.12.

migrated, positions. The curve in Figure 4.14 shows the DMO slownesses measured from the data of figure 4.4. The predicted curve is also shown, and the agreement is reasonably good. The pattern is similar to that of the migration slownesses in Figure 4.7, but shifted and stretched as expected. The measured data are less noisy than the migrated measurements in Figure 4.13, and the agreement with prediction is improved.

4.3 INVERTING THE LINEAR OPERATOR

Singular value decomposition

So far I have discussed the use of $\mathbf{G}$ as a forward modeling operator, for predicting changes in migration slowness caused by specified interval slowness anomalies. How invertible is this operator? The answer to this question will depend on the reflector geometry and the data acquisition geometry. In this section, I consider a variety of reflector and cable geometries and try to invert for the Gaussian anomalies used for modeling in the previous section. In each case, I use the $\mathbf{G}_s$ operator to predict migration slownesses along specified reflectors, and then apply a generalized inverse of $\mathbf{G}_s$ to reconstruct the anomaly. I have parametrized the interval slowness model on a grid of approximately 150 by 200 points, and use only about

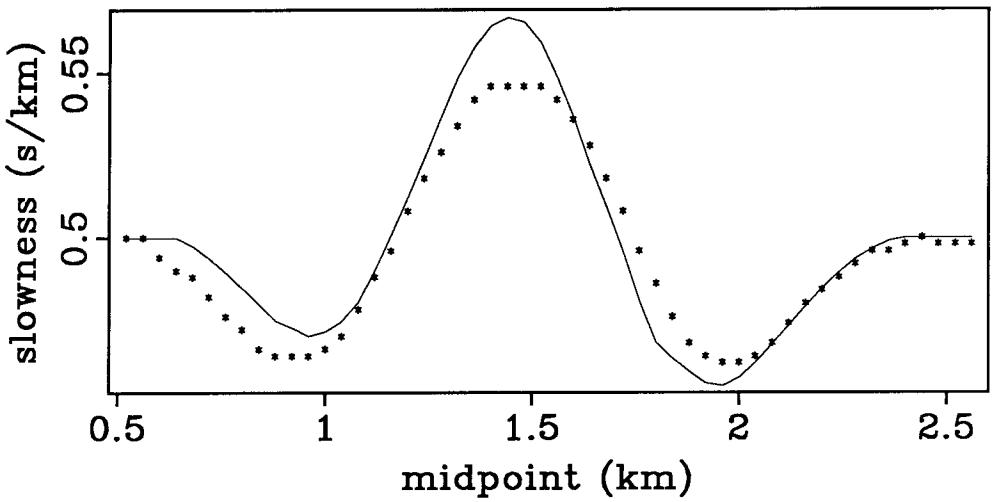

FIG. 4.14. Unmigrated DMO slownesses for the dipping bed in Figure 4.4. The stars are values measured from processing finite-difference synthetic data. The solid curve represents values predicted using the $\mathbf{G}_s$ operator from chapter 3.

200 reflecting points, so the inversion of the $\mathbf{G}_s$ is severely underdetermined. To find a suitable generalized inverse for $\mathbf{G}_s$ I use singular value decomposition (SVD).

The matrix $\mathbf{G}_s$ is generally too large to use SVD, and requires an iterative solution such as conjugate gradients. By using only a few selected reflectors I have been able to apply SVD in the examples here. SVD breaks $\mathbf{G}$ into two orthogonal matrices matrix $\mathbf{U}$ and $\mathbf{V}$ and a diagonal matrix Σ, such that

$$\mathbf{G} = \mathbf{U}\,\Sigma\,\mathbf{V}^T \ . \tag{4.1}$$

This decomposed form provides extensive information about what parts of the problem are resolvable, and what parts are not. The columns of $\mathbf{U}$ (the left singular vectors) provide an orthonormal basis for the data space and the columns of $\mathbf{V}$ (the right singular vectors) an orthonormal basis for the model space. The diagonal entries in Σ (the singular values) are positive or zero. The right singular vectors corresponding to singular values that are zero represent components of the model that are not resolvable; the vectors with large singular values are the ones that will dominate the inversion. SVD also provides an explicit solution for the least squares pseudoinverse of $\mathbf{G}$,

$$\mathbf{G}^{-g} = \mathbf{V}\,\Sigma^{-1}\,\mathbf{U}^T \tag{4.2}$$

where Σ^{-1} is a diagonal matrix whose nonzero elements are the reciprocals of the

nonzero elements of Σ. SVD thus provides for rectangular, singular matrices a decomposition functionally analogous to an eigenvalue and eigenvector representation of a nonsingular operator. For further description of the properties of SVD and the pseudoinverse, see Menke (1984) or Golub and Van Loan (1983).

A single flat bed

The first inversion I consider is of the model of figure 4.1. The result of applying the pseudoinverse $\mathbf{G}_s^{-g}$ to the predicted migration slowness data of figure 4.3 is shown in Figure 4.15. The picture is dominated by two types of artifacts caused by aliasing of the operator. These can be understood by considering Figure 4.16, which shows the $\mathbf{G}_s$ operator for one reflecting point. The coarse sampling of the model space turns the steeply dipping edges of the operator into a set of discrete steps four vertical pixels long. This aliasing pattern is one artifact visible in Figure 4.15. It becomes less for a wider aperture operator, and can be eliminated in practice by smoothing the inverted image. Such smoothing is valid because it is the long wavelength components of the model space that are the goal of the inversion. The second result of operator aliasing occurs because the operator becomes extremely narrow near the reflector, and cannot be represented accurately on the grid of anomaly points. Unfortunately, this is also where the operator has peak amplitude. The inversion is trying to solve for more model points than there are data points, and so it has to choose between many possible solutions. One possible interval slowness model to explain the anomalous pattern of migration slownesses consists of localized, high amplitude anomalies situated immediately above the reflector. Because the operator is represented so inaccurately close to the reflector, this incorrect solution dominates the correct model of a more distant anomaly. A simple way to ameliorate this problem is to taper or truncate the operator close to the reflector. This approach works adequately in practice but is not wholly satisfactory, because there is no a priori way of knowing that an anomaly is not, in fact, located close to a particular reflector. If many reflectors are present, this problem lessens, as I show in section 4.4.

Reducing operator aliasing artifacts

Figure 4.17 shows another inversion of the model of Figure 4.1. This time a 2 km cable is used, the operator is truncated near the reflector, and the inverted result is low-pass filtered, with a cutoff wavelength of 200 m both vertically and horizontally. Most of the artifacts of Figure 4.15 are gone. The anomaly is correctly located

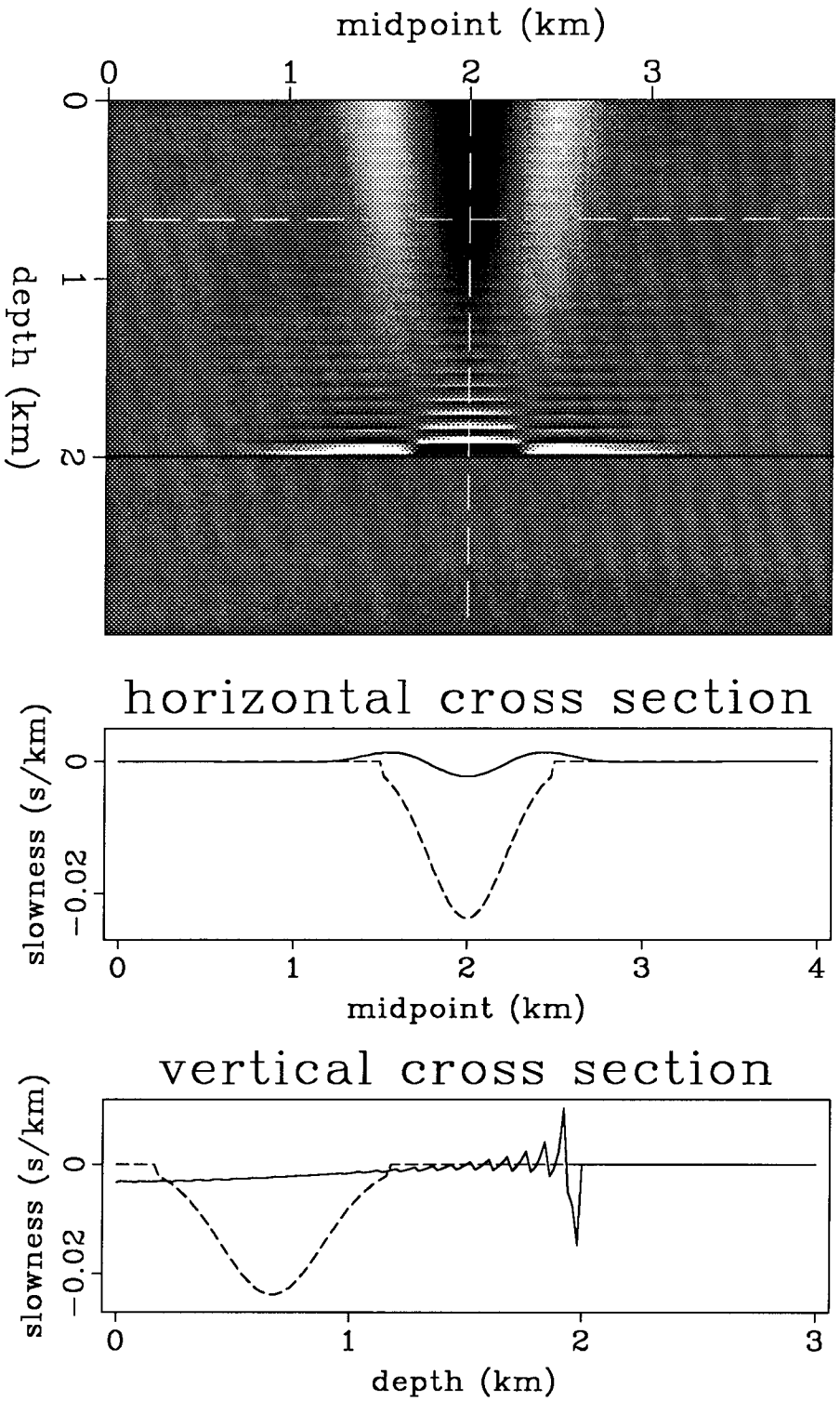

FIG. 4.15. Result of forward modeling and inverting the $\mathbf{G}_s$ operator using the flat bed model of Figure 4.1. The cable length is 1 km. The top picture shows the inverted anomalous interval slowness field. The lower figures show vertical and horizontal cross sections through the center of the Gaussian anomaly. Input values of the anomaly are shown as dashed lines for comparison.

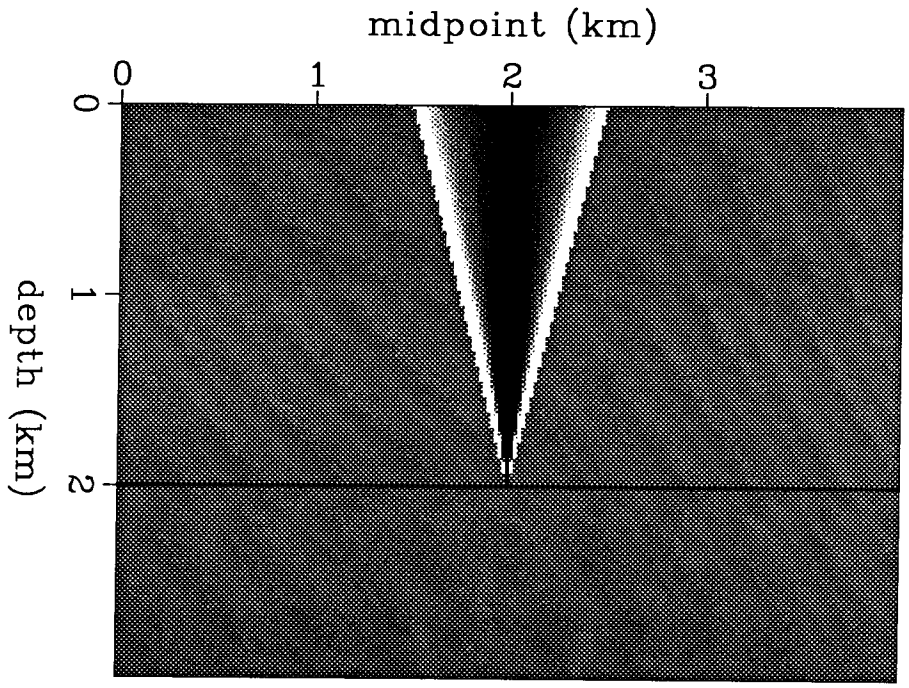

FIG. 4.16. Example of the $\mathbf{G}_s$ operator used in the inversion of Figure 4.15. Note the aliased "stair steps" along the edge of the operator, and the inaccuracy of the representation of the operator near the reflecting point.

horizontally, but is smeared vertically, perpendicular to the reflecting bed. This smearing arises because most of the rays are traveling nearly vertically, and is a common feature of tomographic inversions. Because the energy is smeared over a broader area than that of the original anomaly, the peak amplitude in the inversion is also lower.

The most interesting feature of Figure 4.17 is the presence of positive sidelobes on either side of the central negative peak in the inversion. This resonance is clearly visible in the horizontal cross section. The origin of this resonance can be understood by examining the singular value spectrum shown in Figure 4.18. The spectrum contains 200 non-zero values, corresponding to the number of reflecting points used. The spectrum decays rapidly, so the inversion is dominated by the first few model-space singular vectors. The first two of these vectors are shown at the top of Figure 4.19. These singular vectors form a pair of phase-shifted sinusoids laterally. Clearly, the inversion is most sensitive to this particular lateral wavelength. Smaller singular values correspond to shorter lateral and vertical wavelengths, as shown in the lower

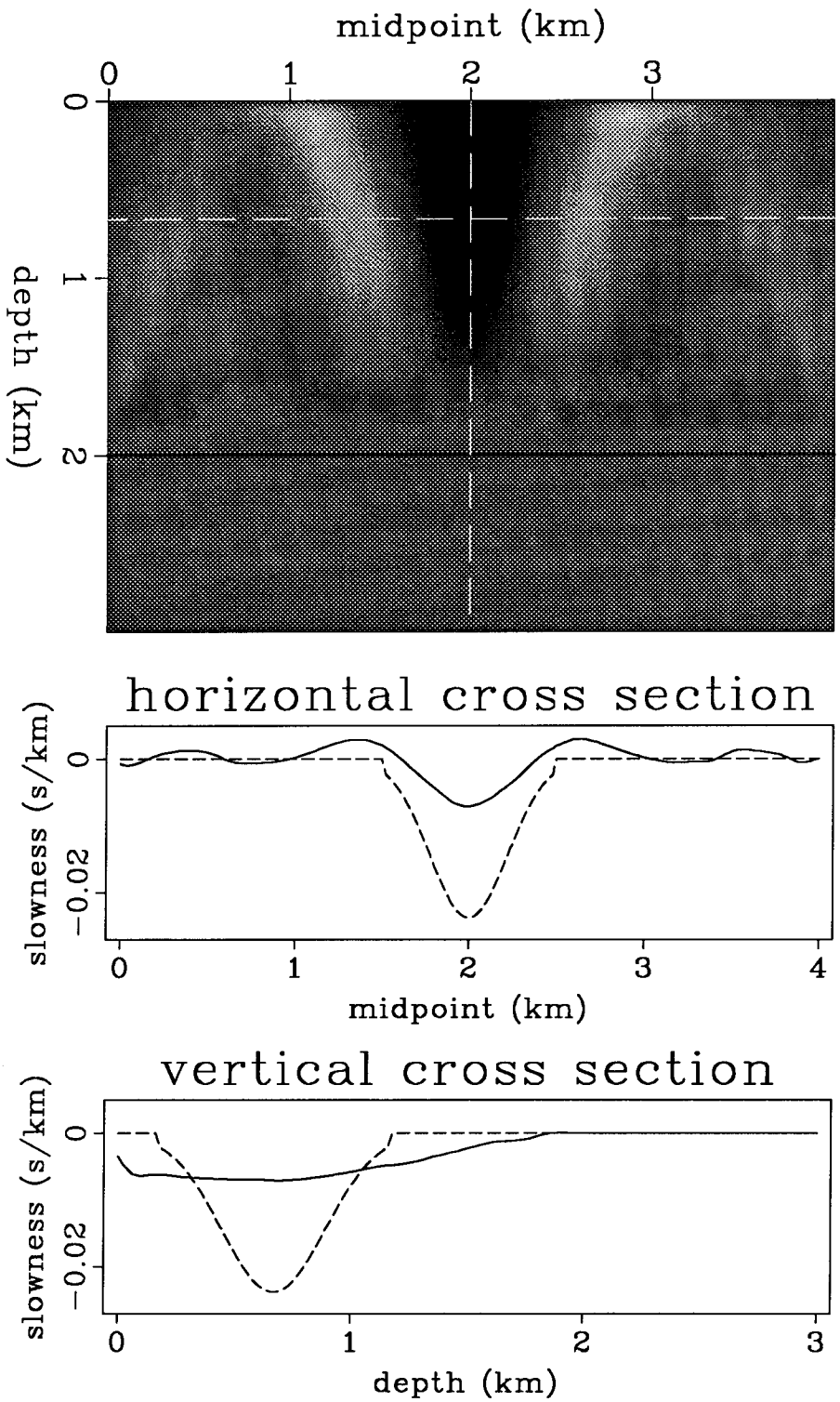

FIG. 4.17. Result of forward modeling and inverting the $\mathbf{G}_s$ operator using the flat bed model of Figure 4.1. The cable length is 2 km. The operator is truncated close to the reflector, and the inverted image is low pass filtered. The top picture shows the inverted anomalous interval slowness field. The lower figures show vertical and horizontal cross sections through the center of the Gaussian anomaly. Input values of the anomaly are shown as dashed lines for comparison.

pictures in Figure 4.19 and in Figure 4.20. As the wavenumber content increases, the singular vectors resemble bandlimited combinations of the backprojection "V" patterns determined by the aperture of the operator.

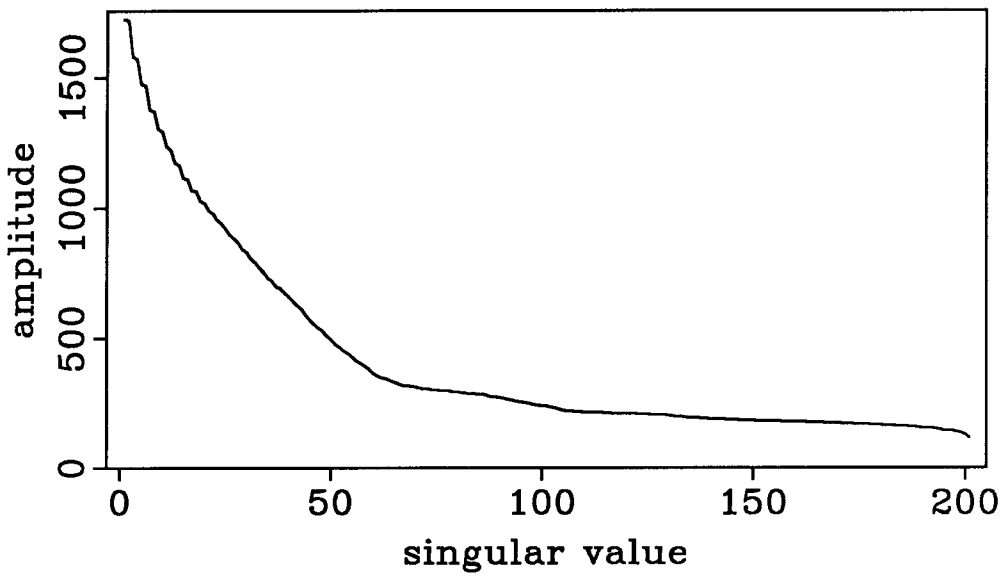

FIG. 4.18. Singular value spectrum of the $\mathbf{G}_s$ operator used in the inversion shown in Figure 4.17.

This singular value structure, and the corresponding frequency domain transfer functions, have been studied in detail by Loinger (1983) and by Toldi (1985). I do not pursue this Fourier domain analysis here, because it is applicable only if both the background slowness field and the reflector structure are laterally invariant, and so does not generalize for reflectors that are dipping.

A single dipping bed

Figure 4.21 shows an inversion for the 20° dipping bed model of Figure 4.4. Again, a 2 km cable is used, the operator is truncated near the reflector, and the inverted result is low-pass filtered, with a cutoff wavelength of 200 m both vertically and horizontally. The result is very similar to that shown in Figure 4.17 for the flat bed model, but skewed by the dip. The center of the anomaly is correctly located. The anomaly is smeared perpendicular to the reflecting bed, but is well resolved parallel to it, except for sidelobes similar to those seen in Figure 4.17. The singular value spectrum of the dipping $\mathbf{G}_s$ operator is shown in Figure 4.22. It differs little

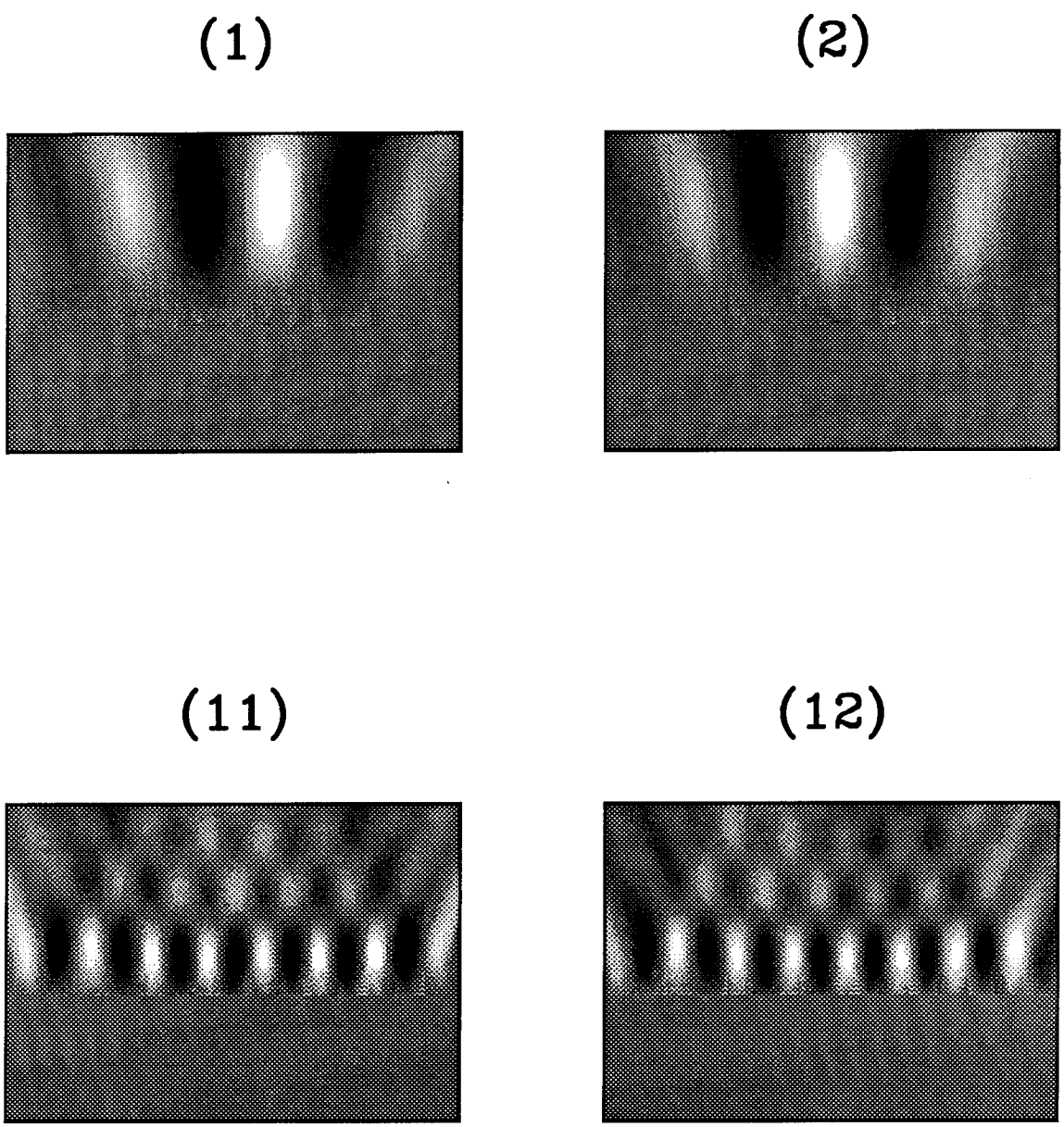

FIG. 4.19. Selected model space singular vectors for the $\mathbf{G}_s$ operator used in the inversion shown in Figure 4.17. The singular vector numbers correspond to the singular values in Figure 4.18. The axes of the plots are the same as for the model in Figure 4.1 and the inversion in Figure 4.17.

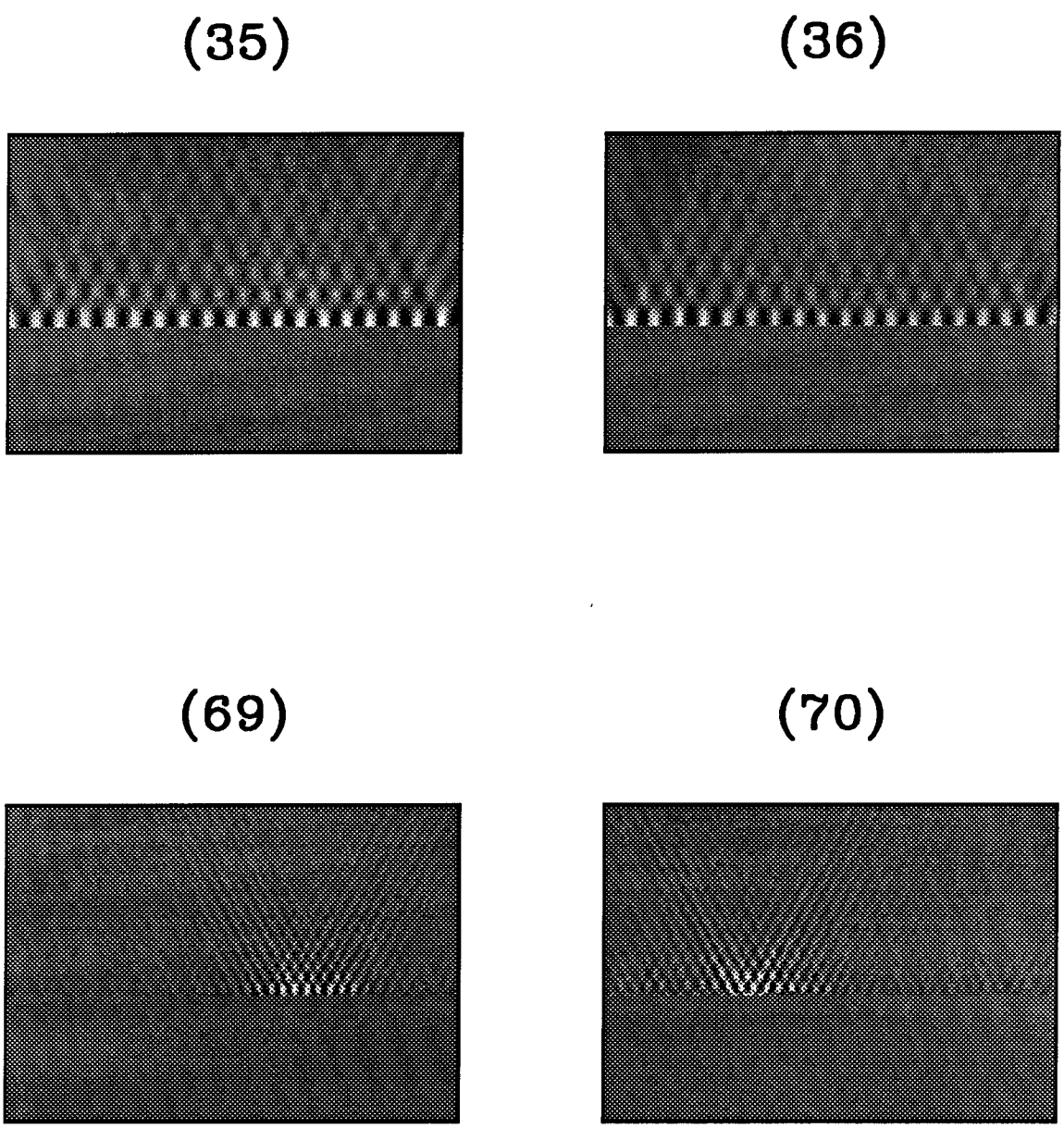

FIG. 4.20. Selected model space singular vectors for the $\mathbf{G}_s$ operator used in the inversion shown in Figure 4.17. The singular vector numbers correspond to the singular values in Figure 4.18. The axes of the plots are the same as for the model in Figure 4.1 and the inversion in Figure 4.17.

from that of the flat bed operator in Figure 4.18. Selected model-space singular vectors are shown in Figure 4.23 and 4.24. Again, they are similar to those for the flat bed operator, but now the effective angular aperture of the operator increases as one moves updip, and the dominant wavelengths in the singular vectors correspondingly increase, as can be seen particularly well in vectors 29 and 30 in Figure 4.24.

A comparison with ray-trace tomography

How good are these inversions? Clearly, the anomalies are not reconstructed perfectly. Is this a failure of the particular inversion method used here, or is it intrinsic to using a single reflector and a shooting geometry with limited aperture and view angle? The best comparison is with conventional ray-trace tomography. In ray-trace tomography, traveltimes are computed for all shot-geophone pairs, and the entire set of traveltime is inverted. In the migration slowness inversion of Figures 4.17 and 4.21, the traveltime perturbations for a given midpoint are all combined into one effective parameter, the migration slowness, describing the curvature of the best fitting moveout curve. Ray-trace tomography thus uses more detailed information. As discussed in section 3.3, migration slowness analysis can be posed as a filtered form of tomography. This filter cannot add information, so ray-trace tomography defines the resolution limit for analyzing these synthetic examples.

Figure 4.25 shows the result of forward modeling rays using the dipping bed model of Figure 4.4, and inverting the traveltime data using an iterative tomographic algorithm (Stork, 1988). The cable length used is 2 km, the same as in Figure 4.21. The anomaly is again well resolved parallel to the reflector, and broadly smeared perpendicular to it. The extent of the anomaly is better defined, but otherwise the reconstruction is substantially the same as that achieved using migration slownesses. The principal improvement of this image over the migration slowness inversion of Figure 4.21 is the near absence of resonant sidelobes.

Inverting DMO slownesses

I have claimed in section 3.10 that DMO slownesses contain the same information as migration slowness. Analysis of the dipping bed finite-difference synthetic example in section 4.2 suggested that DMO slowness anomalies might be more robust to measure than the corresponding migration slowness anomalies. The underlying $\mathbf{G}_s$ operator is the same for both DMO slownesses and migration slownesses, so the inversion should be the same. Figure 4.26 shows the result of inverting the DMO slownesses predicted for the 20° dipping bed of Figure 4.4. As expected, the

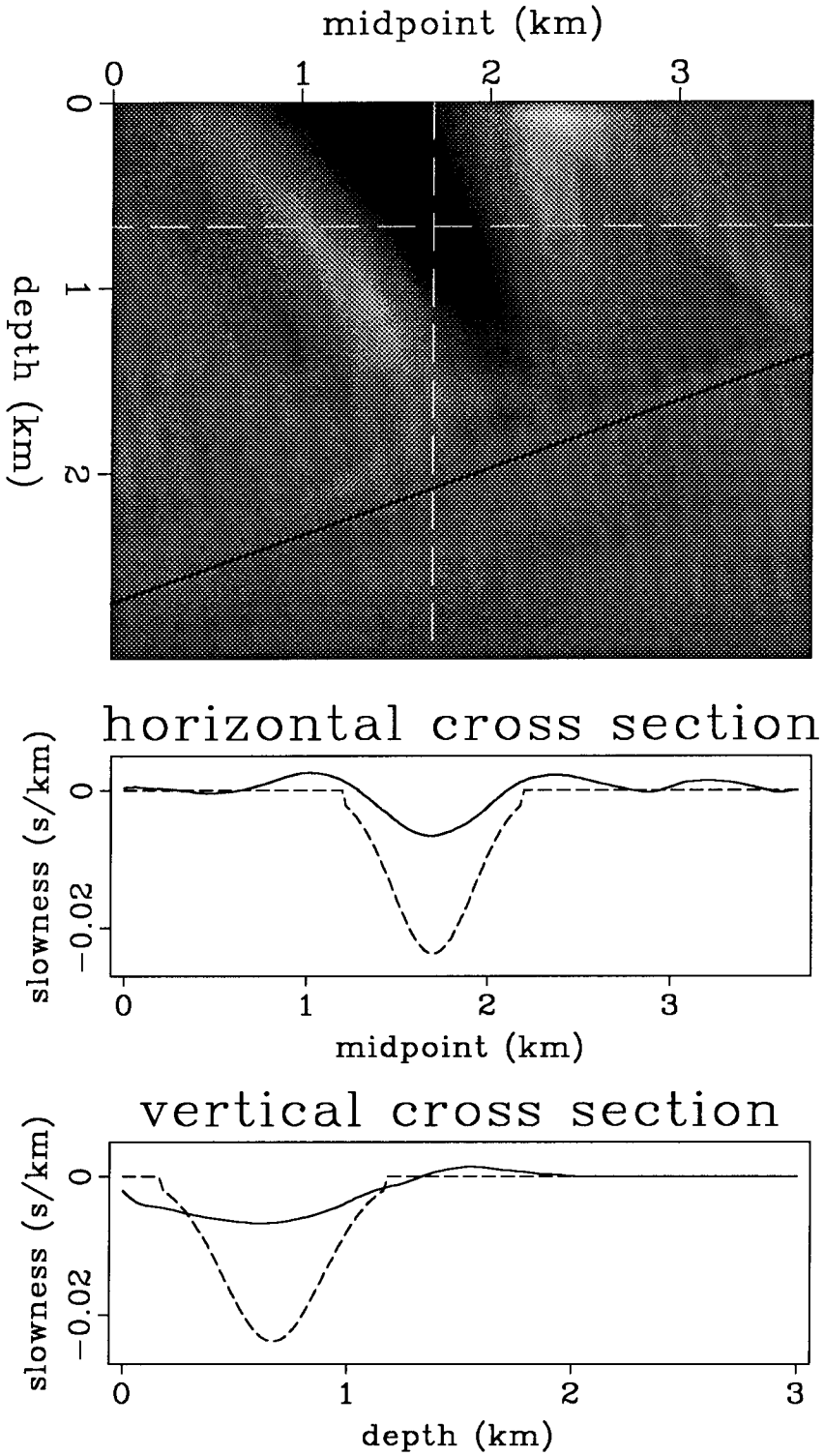

FIG. 4.21. Result of forward modeling and inverting the $\mathbf{G}_s$ operator using the 20° dipping bed model of Figure 4.4. The cable length is 2 km. The top picture shows the inverted anomalous interval slowness field. The lower figures show vertical and horizontal cross sections through the center of the Gaussian anomaly. Input values of the anomaly are shown as dashed lines for comparison.

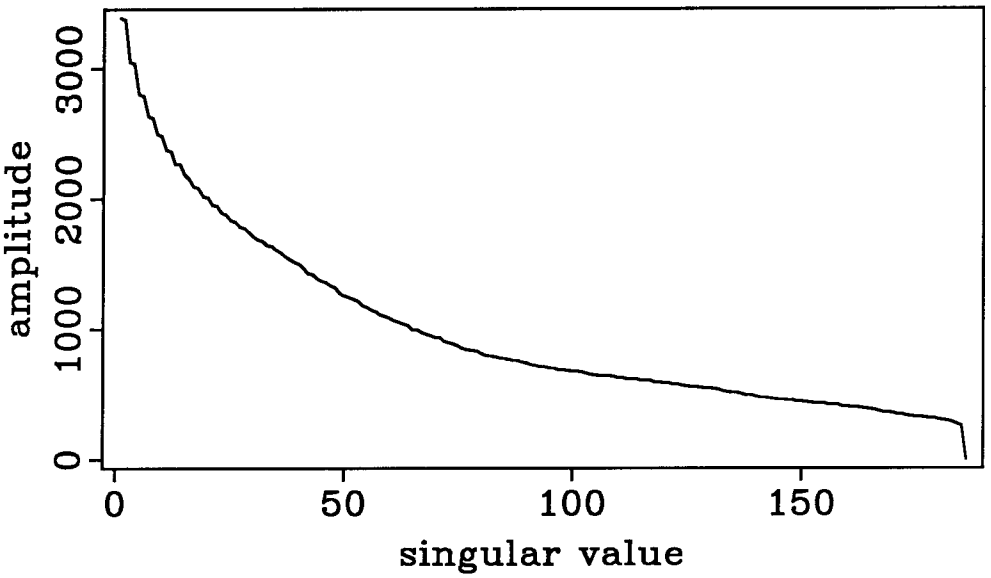

FIG. 4.22. Singular value spectrum of the $\mathbf{G}_s$ operator used in the inversion shown in Figure 4.21.

inverted result is indistinguishable from that obtained in Figure 4.21 using migration slownesses.

Inverting slowness anomalies measured from synthetic model data

The slowness anomalies measured from the finite-difference data for the dipping bed model (Figures 4.13 and 4.14) generally agree with the predicted values, but differ in the peak amplitude of the anomaly and in the amount of asymmetry seen in the anomaly pattern, as well as being contaminated with picking errors. How well can these measured values be inverted?

Figure 4.27 shows the result of inverting the measured migration slownesses from Figure 4.13. This inversion cannot be compared directly with that shown in Figure 4.21, because the cable length for the finite-difference data (1 km) is only half that used in Figure 4.21. A better comparison is provided in Figure 4.28, which shows the result of forward prediction and inversion with a $\mathbf{G}_s$ operator using the shorter cable length. The shorter cable results in a narrower angular aperture, and poorer resolution of the anomaly. The inversion of the measured data (Figure 4.27) has noticeably larger artifacts than the inversion of the predicted data (Figure 4.28), but still yields a reasonable resolution of the anomaly. Figure 4.29 shows the result of inverting the measured DMO slownesses from Figure 4.14. These data are less noisy than the migration data of Figure 4.13, and the resulting inversion is

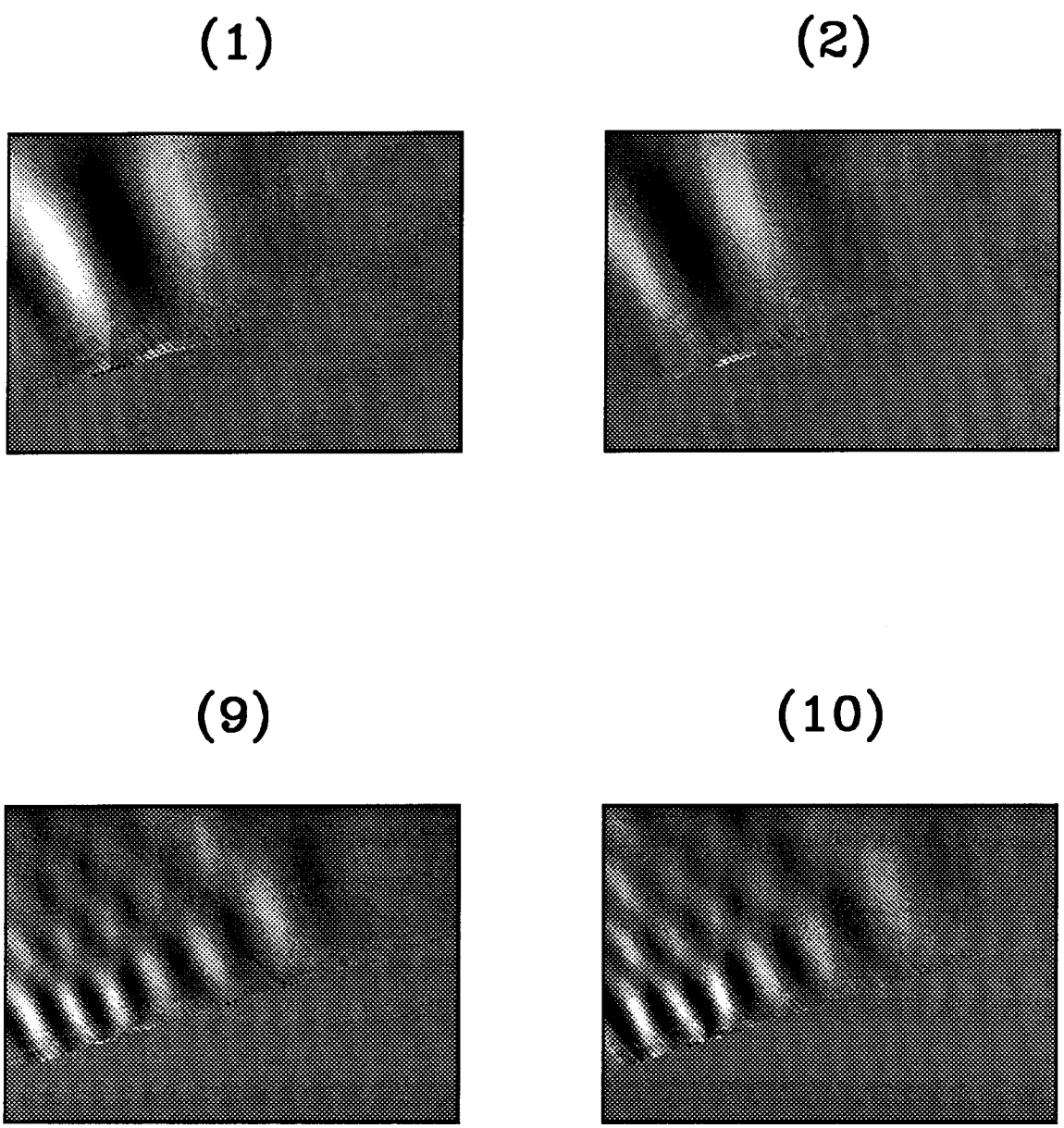

FIG. 4.23. Selected model space singular vectors for the $\mathbf{G}_s$ operator used in the inversion shown in Figure 4.21. The singular vector numbers correspond to the singular values in Figure 4.22. The axes of the plots are the same as for the model in Figure 4.4 and the inversion in Figure 4.21.

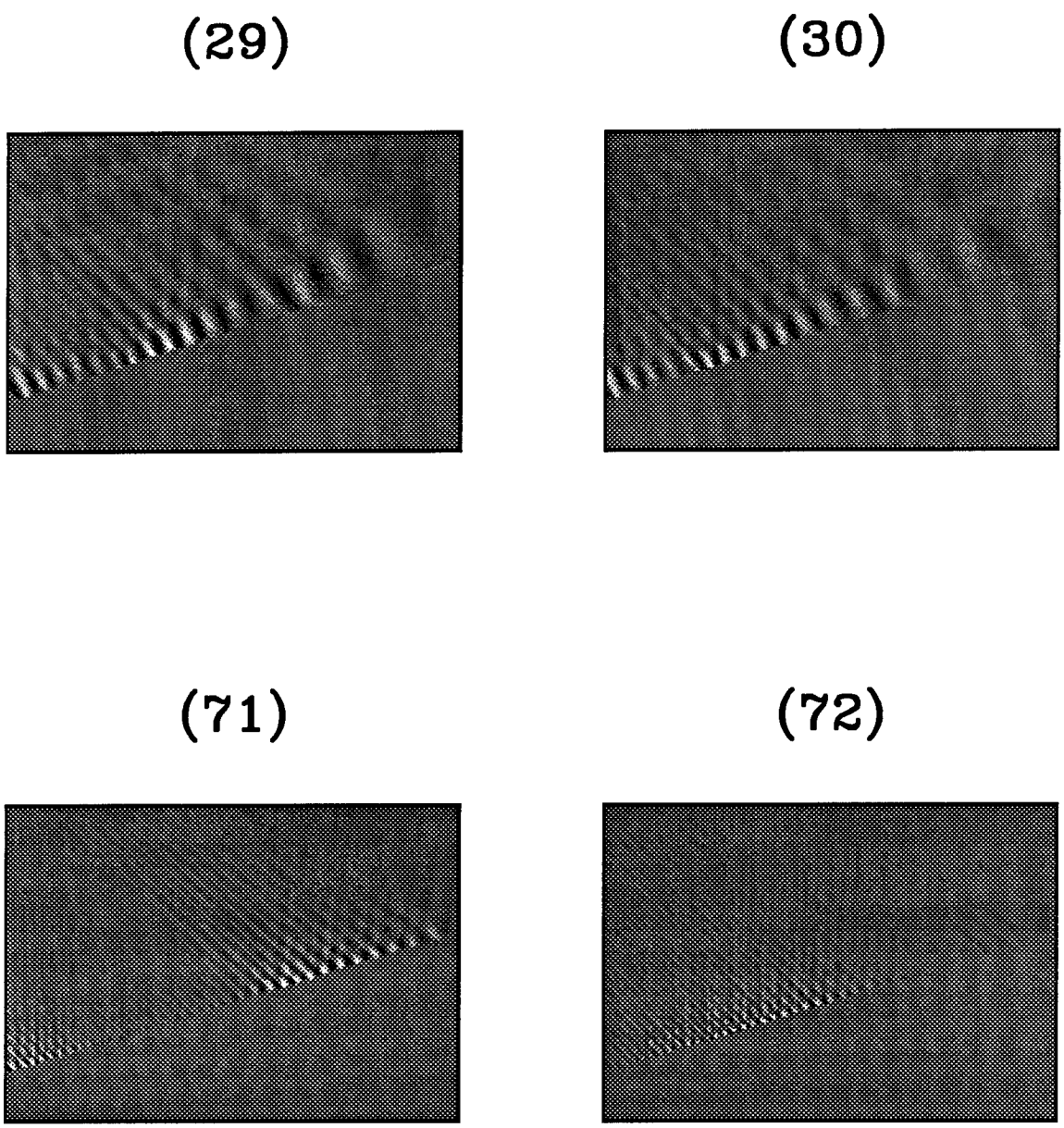

FIG. 4.24. Selected model space singular vectors for the $\mathbf{G}_s$ operator used in the inversion shown in Figure 4.21. The singular vector numbers correspond to the singular values in Figure 4.22. The axes of the plots are the same as for the model in Figure 4.4 and the inversion in Figure 4.22.

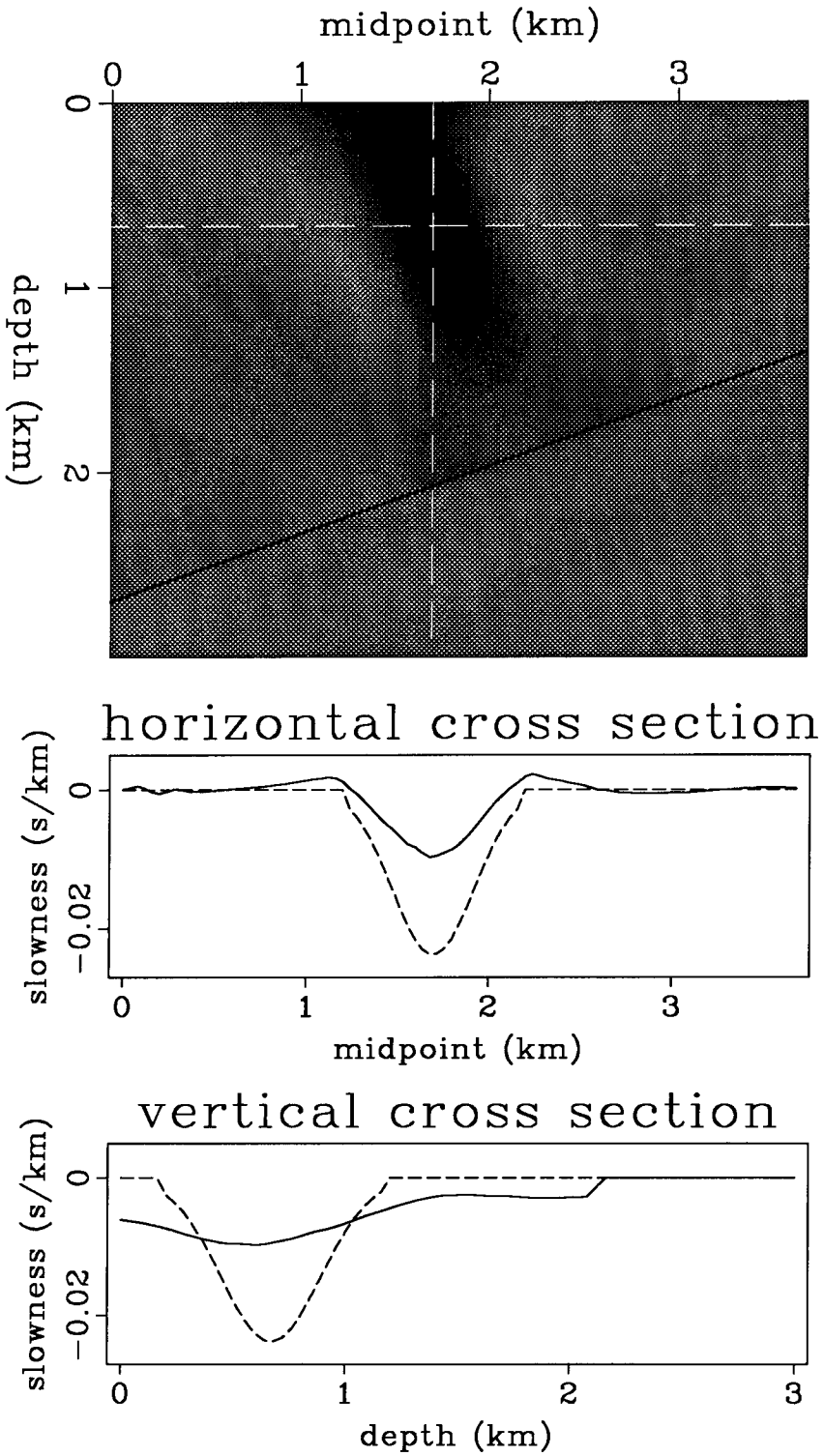

FIG. 4.25. Result of ray-trace tomographic inversion using the dipping bed model of Figure 4.4. The cable length is 2 km. The top picture shows the inverted anomalous interval slowness field. The lower figures show vertical and horizontal cross sections through the center of the Gaussian anomaly. Input values of the anomaly are shown as dashed lines for comparison. The tomographic inversion data for this figure were generously provided by Christof Stork.

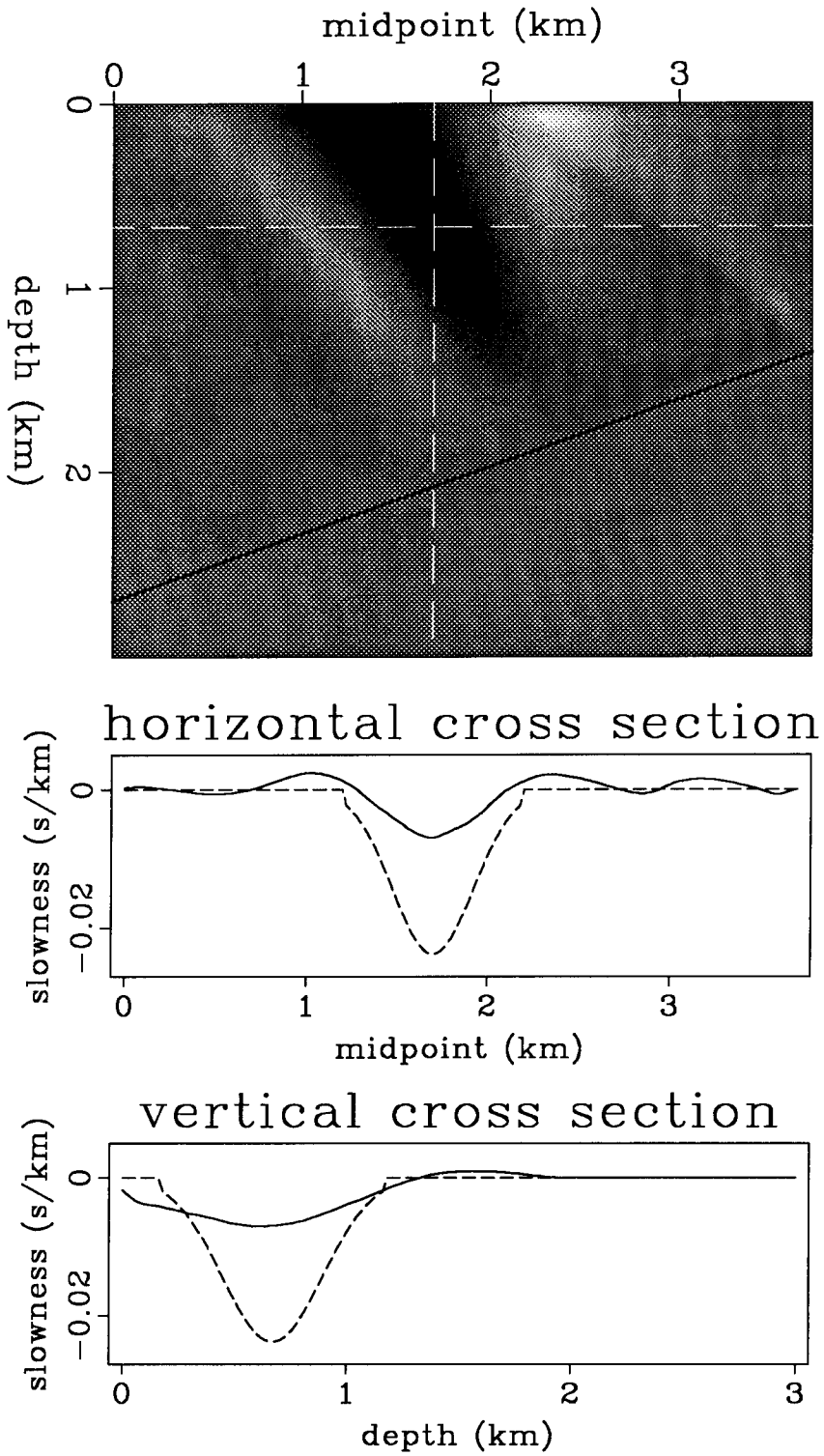

FIG. 4.26. Result of forward modeling and inverting DMO slownesses for the 20° dipping bed model of Figure 4.4. The cable length is 2 km. The top picture shows the inverted anomalous interval slowness field. The lower figures show vertical and horizontal cross sections through the center of the Gaussian anomaly. Input values of the anomaly are shown as dashed lines for comparison. This figure is nearly identical to Figure 4.21, which used migration slownesses for the same model.

correspondingly better, with the anomaly resolved nearly as well as in Figure 4.28.

4.4 IMPROVING (AND DEGRADING) RESOLUTION

Three parallel dipping reflectors

How can the results of the preceding section be improved? The are two basic paths open: more reflectors, or a more sophisticated inversion. I look first at the effects of improving the resolution by using more than a single planar bed to illuminate the anomaly. This will ordinarily be the most important contribution to improved velocity analysis; good velocity resolution in practice depends on favorable geologic structure as much or more than on geophysicists' ingenuity.

Figure 4.30 shows an inversion using three parallel dipping reflectors in place of the single one used in Figure 4.17; beds have been added 400 m above and below the single reflector previously used. The cable length is again 2 km, and the anomaly is the same one as in Figure 4.4. The lower edge of the anomaly is better defined, but the image remains smeared perpendicular to the beds, and the sidelobes are similar to the single bed inversion. Note that this time I did not truncate the operator near the beds. The redundant information from the multiple beds forces the inversion to reject a model with strong anomalies along the beds in favor of a concentrated anomaly located above all the beds. Thus, the effect seen in Figure 4.15 should not be a problem in practice.

Three reflectors with different dips

The smearing and the sidelobe resonance are both caused in large part by using only a single dip angle on the reflectors, limiting the directions in which the anomaly is illuminated. Both of these problems are dramatically reduced if reflectors are located so that rays traverse the anomaly in a wide range of directions. Figure 4.31 shows an inversion of the same anomaly as in Figures 4.17, but using three beds of different dip. The inversion is much better than any of the previous results. The peak is circular and correctly located, although it is still a little low in amplitude and some small sidelobes can still be seen in the horizontal cross section. Thus, favorable geological structure with reflectors situated so that anomalies are illuminated from many angles is the most important single factor contributing to good velocity resolution.

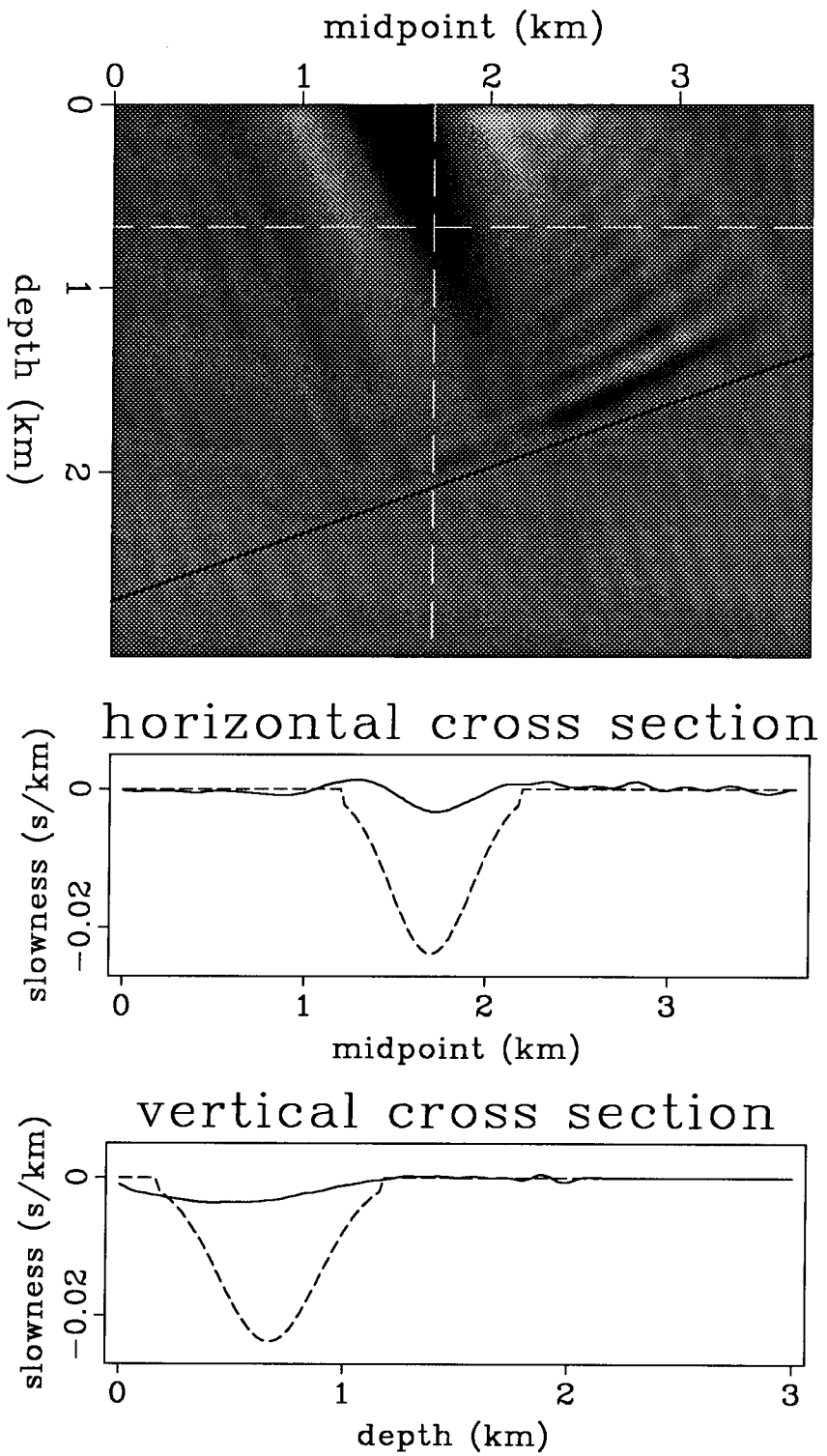

FIG. 4.27. Result of inverting the migration slownesses from Figure 4.13, measured from finite-difference synthetic data for the 20° dipping bed model of Figure 4.4. The cable length is 1 km. The top picture shows the inverted anomalous interval slowness field. The lower figures show vertical and horizontal cross sections through the center of the Gaussian anomaly. Input values of the anomaly are shown as dashed lines for comparison.

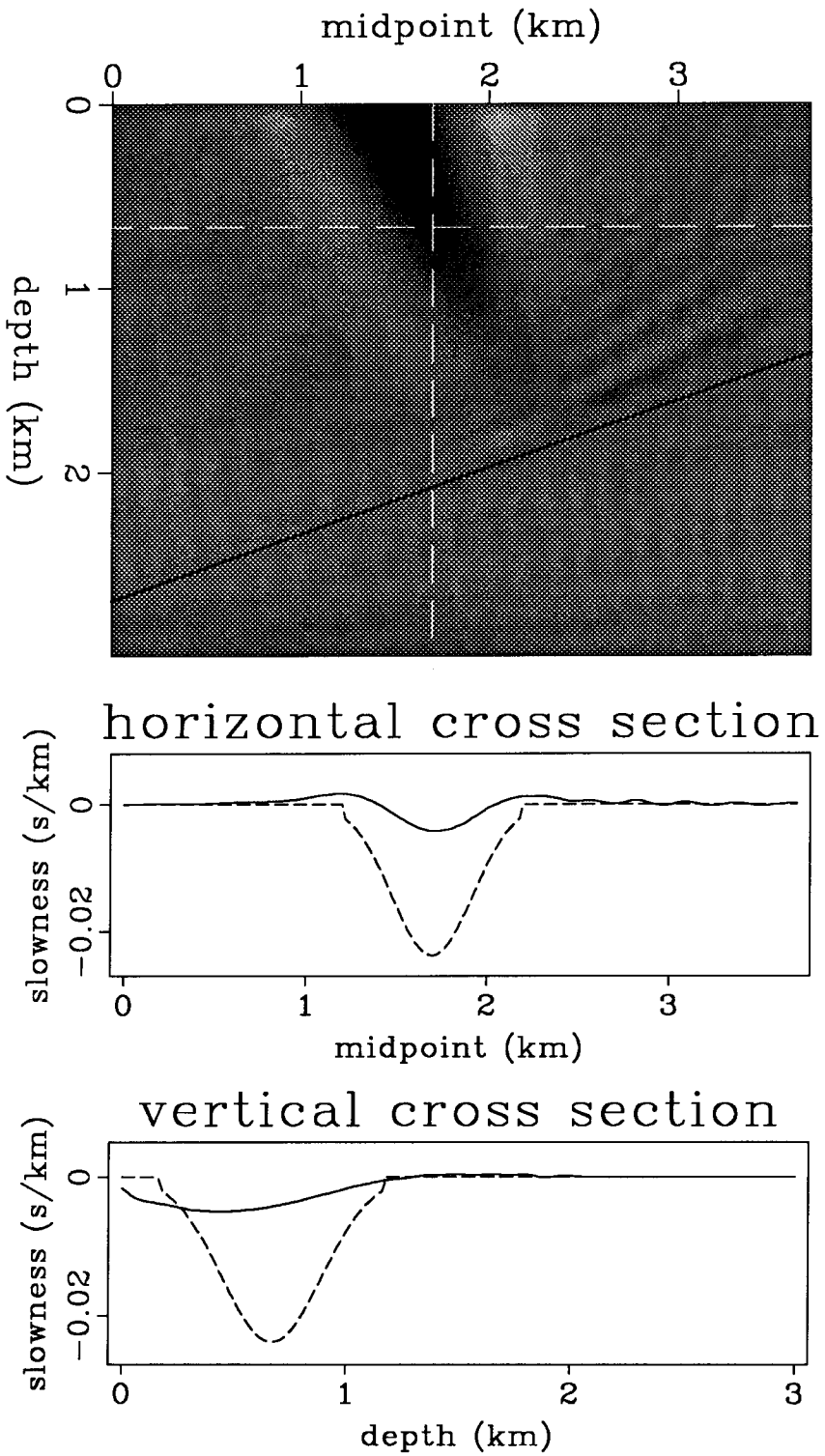

FIG. 4.28. Result of forward modeling and inverting the $\mathbf{G}_s$ operator using a 1 km cable. The anomaly model is that of Figure 4.4. The top picture shows the inverted anomalous interval slowness field. The lower figures show vertical and horizontal cross sections through the center of the Gaussian anomaly. Input values of the anomaly are shown as dashed lines for comparison.

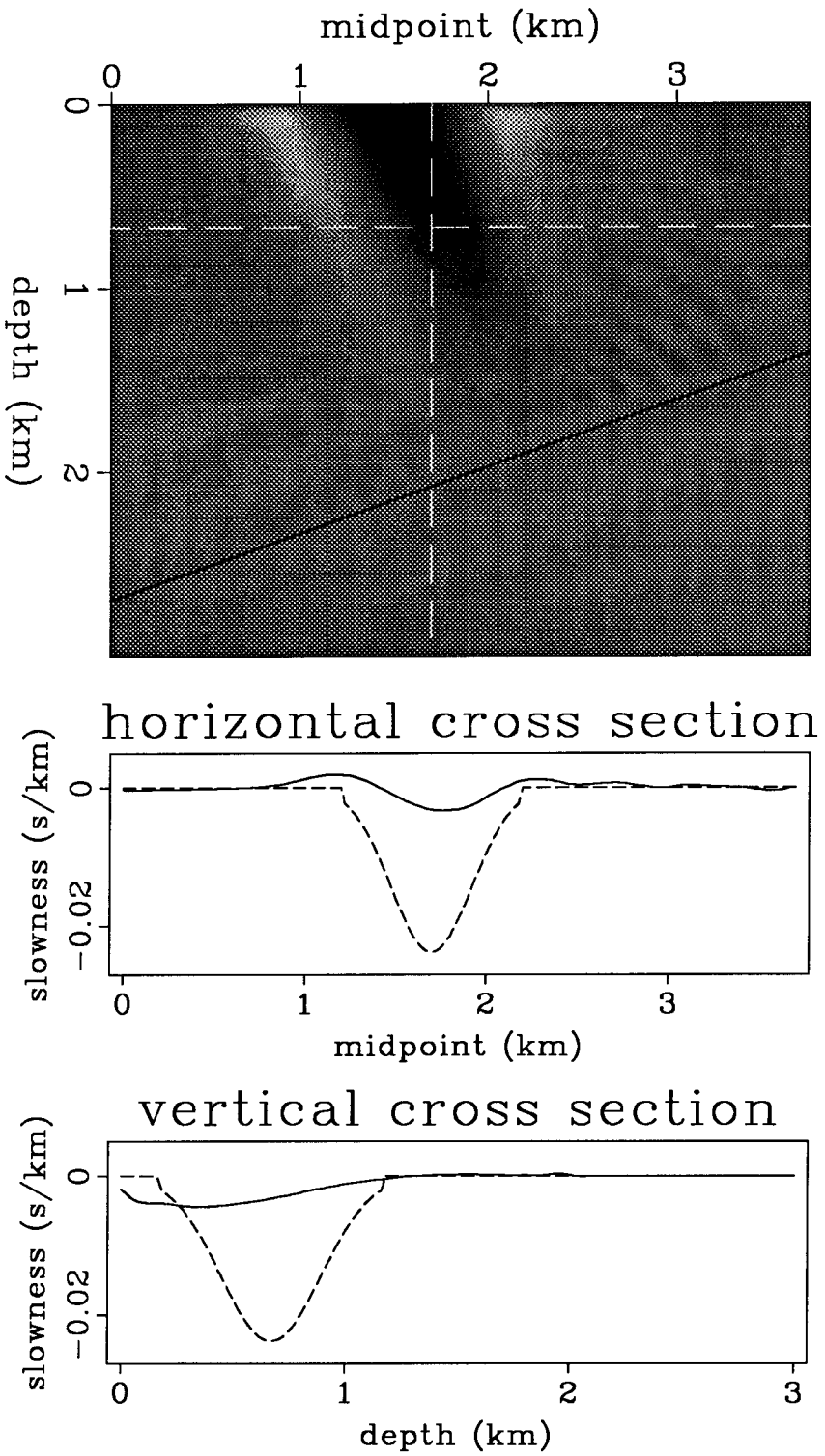

FIG. 4.29. Result of inverting the DMO slownesses from Figure 4.14, measured from finite-difference synthetic data for the 20° dipping bed model of Figure 4.4. The cable length is 1 km. The top picture shows the inverted anomalous interval slowness field. The lower figures show vertical and horizontal cross sections through the center of the Gaussian anomaly. Input values of the anomaly are shown as dashed lines for comparison.

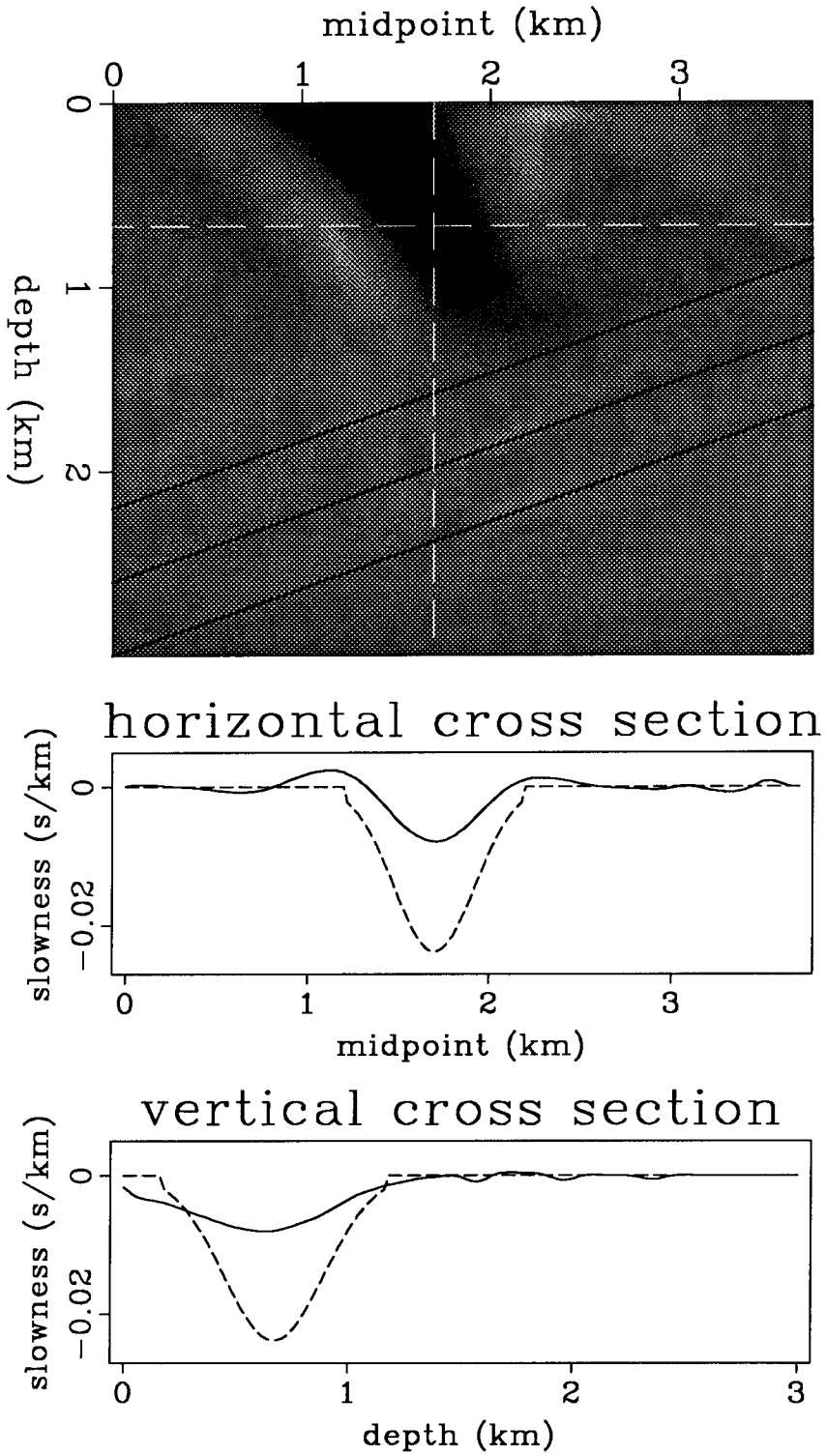

FIG. 4.30. Result of forward modeling and inverting the $\mathbf{G}_s$ operator using three parallel dipping beds. The anomaly is the same as in Figure 4.4. The cable length is 2 km. The operator is not truncated close to the reflector. The top picture shows the inverted anomalous interval slowness field. The lower figures show vertical and horizontal cross sections through the center of the Gaussian anomaly. Input values of the anomaly are shown as dashed lines for comparison.

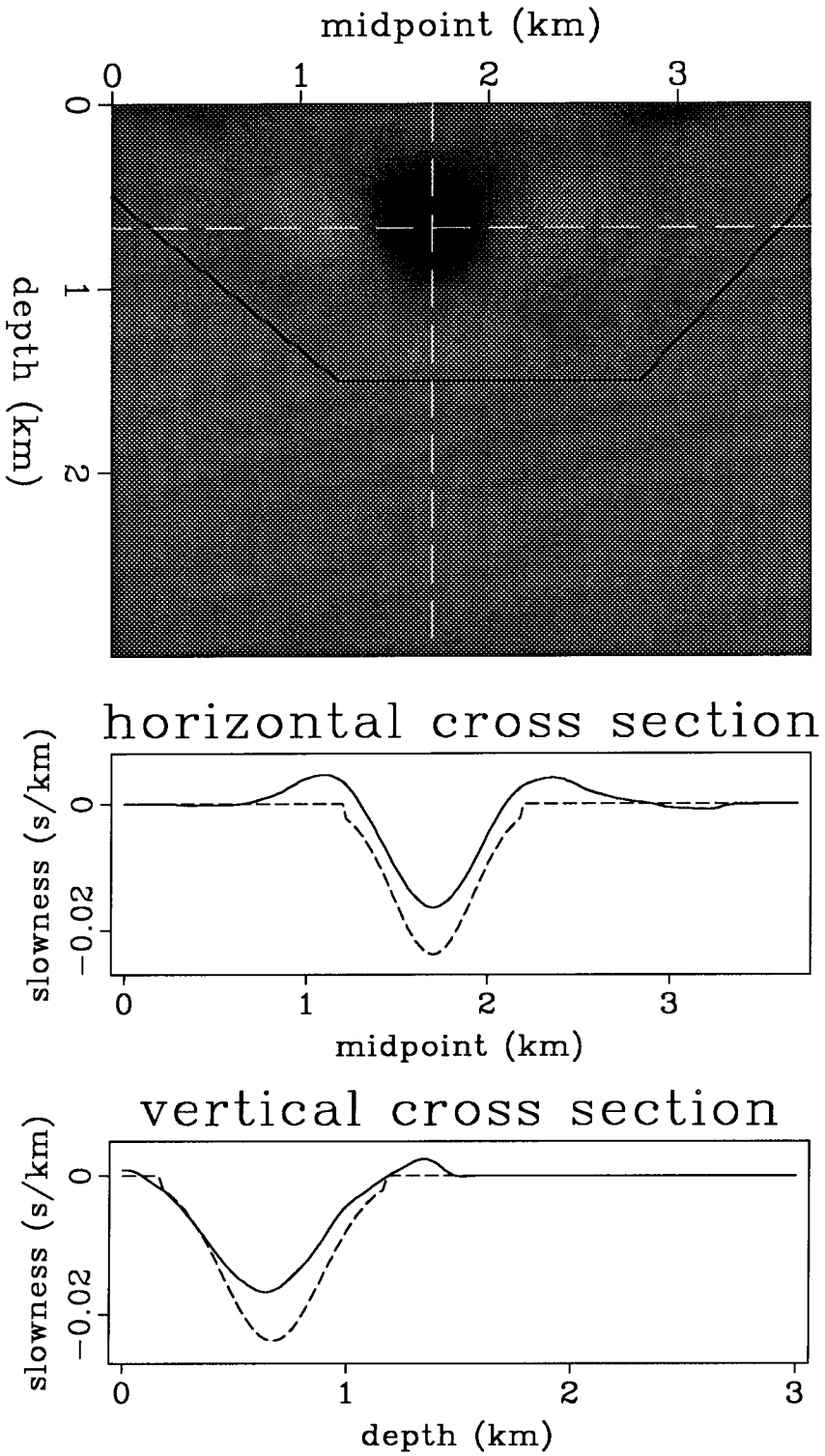

FIG. 4.31. Result of forward modeling and inverting the $\mathbf{G}_s$ operator using three beds with different dips. The anomaly is the same as in Figure 4.4. The cable length is 2 km. The top picture shows the inverted anomalous interval slowness field. The lower figures show vertical and horizontal cross sections through the center of the Gaussian anomaly. Input values of the anomaly are shown as dashed lines for comparison.

Joint inversion using inner and outer offsets separately

The wavelength of the sidelobe resonance is controlled by the cable length, which determines the aperture of the $\mathbf{G}_s$ operator. This suggests that it might be possible to damp the resonance by performing a joint inversion using cables of different lengths. Alternatively, one can divide the cable into sections, and jointly invert the data from each section. Figures 4.32 through 4.34 show the result of splitting the cable into inner and outer halves, inverting each, and jointly inverting. The model used is the dipping bed of Figure 4. The cable is 2 km long; one operator uses the inner 1 km, and the other the outer 1 km. Figure 4.32 shows the migration slowness anomalies predicted by each operator. Also shown for comparison is the response using the 2 km cable of Figure 4.15. The inversion using the 1 km cable has already been shown in Figure 4.28. Figure 4.33 also uses a 1 km aperture, but the inner offset is 1 km, so it is equivalent to using the outer half of the 2 km cable used in Figure 4.21. Figure 4.34 shows the joint inversion of the two operators.

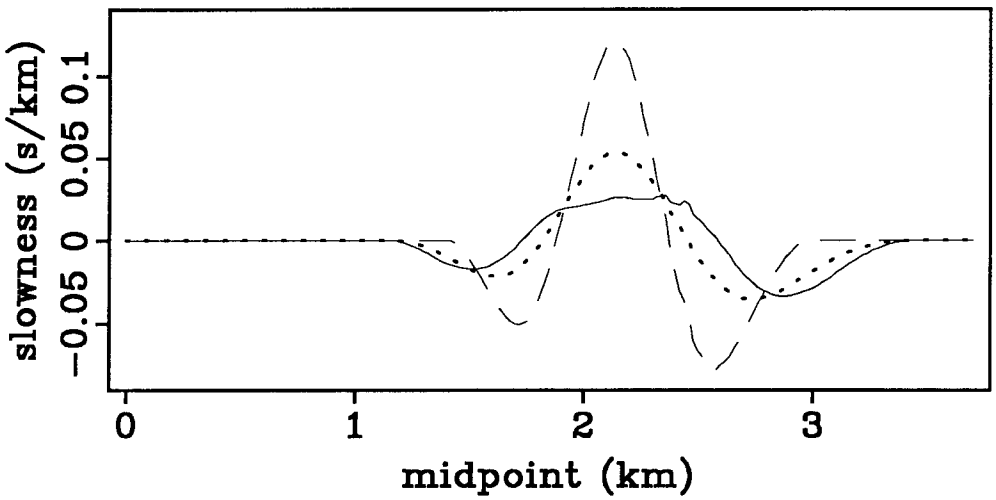

FIG. 4.32. Migration slownesses for the dipping bed model of Figure 4. The dashed curve is the prediction using the inner 1 km of the cable. The solid curve is the prediction using the outer 1 km of the cable. The dotted curve is the prediction using the full 2 km cable.

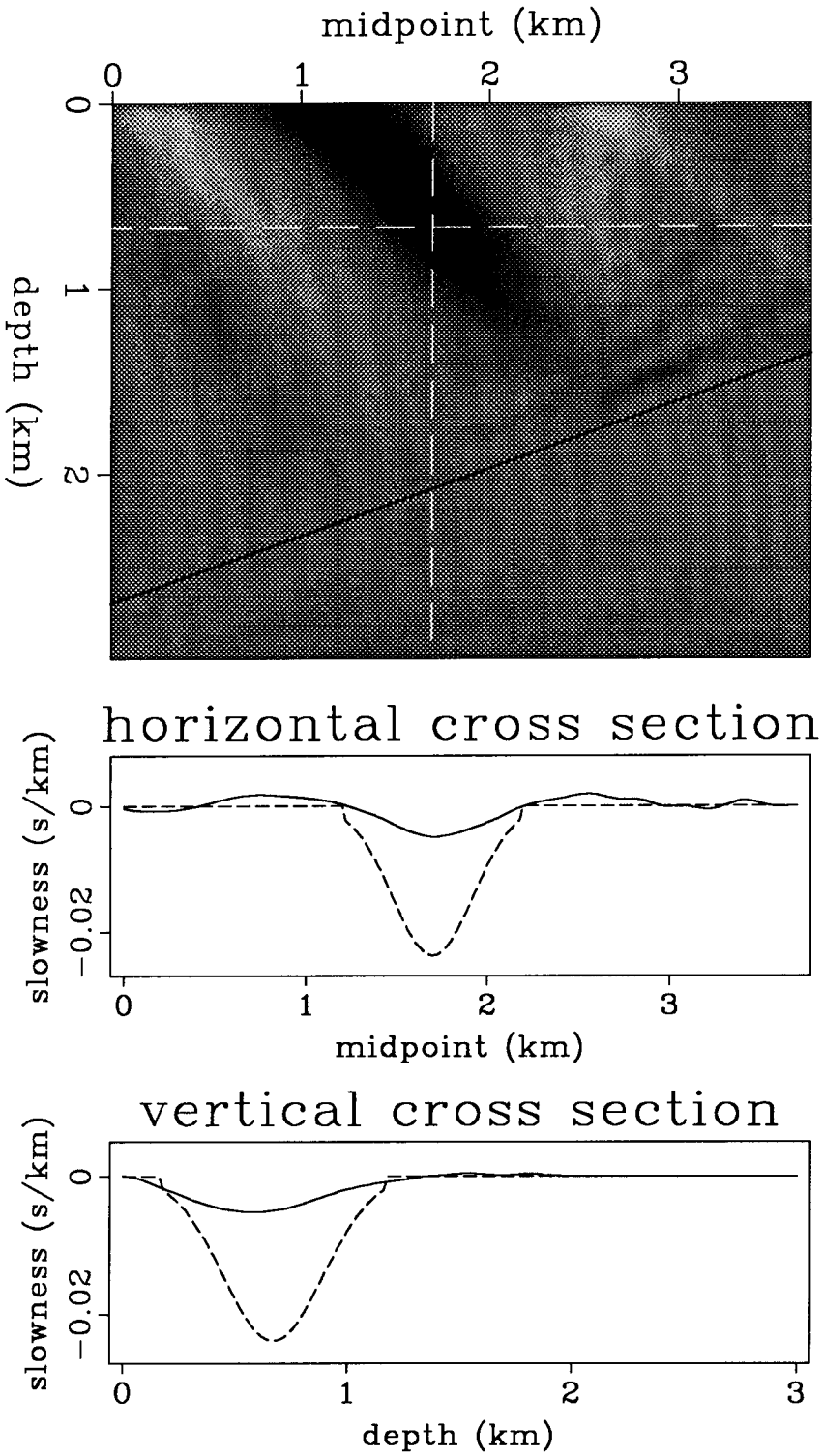

FIG. 4.33. Result of forward modeling and inverting the $\mathbf{G}_s$ operator using a 1 km cable with 1 km inner offset. The anomaly model is that of Figure 4.4. The top picture shows the inverted anomalous interval slowness field. The lower figures show vertical and horizontal cross sections through the center of the Gaussian anomaly. Input values of the anomaly are shown as dashed lines for comparison.

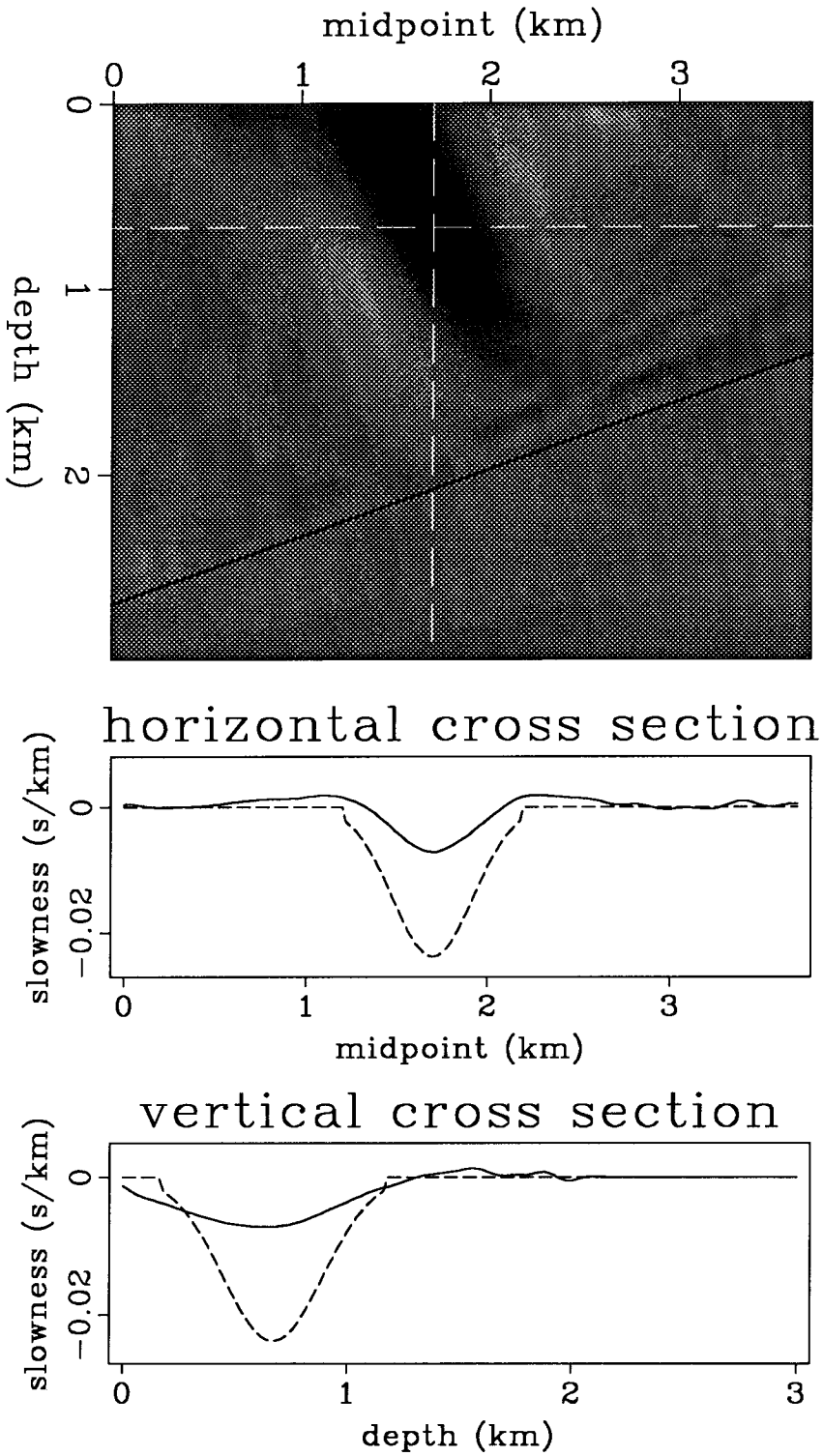

FIG. 4.34. Result of forward modeling and inverting the $\mathbf{G}_s$ operator using inner and outer halves of a 2 km cable. This figure represents a joint inversion of the data used for Figure 4.28 and 4.33. The anomaly model is that of Figure 4.4. The top picture shows the inverted anomalous interval slowness field. The lower figures show vertical and horizontal cross sections through the center of the Gaussian anomaly. Input values of the anomaly are shown as dashed lines for comparison.

The resolution using either the inner or the outer 1 km cable (Figure 4.28 or 4.33, respectively) is considerably poorer than that shown in Figure 4.21, which uses the full 2 km cable. The resolution from the joint inversion (Figure 4.34), however, rivals the tomographic reconstruction in Figure 4.25. For a broad anomaly such as the one used here, the information contained in the complete set of traveltimes for the full offset range is heavily redundant. Nearly as good a reconstruction is achieved here using only two parameters per midpoint (the migration slowness perturbations for inner and outer cables), instead of using all the traveltimes for every offset.

Joint inversion of migration slowness and traveltime anomalies

So far I have considered only the $\mathbf{G}_s$ operator relating perturbations in interval slowness and migration slowness. As discussed in chapter 3, the full $\mathbf{G}$ operator has a second independent part to it, telling how much pullup is observed perpendicular to a bed. For simplicity I consider flat beds, where $\mathbf{G}_y$ is zero, and only $\mathbf{G}_\tau$ needs to be examined. Figure 4.35 shows the traveltime pullup predicted using $\mathbf{G}_\tau$ for a 1 km cable and the model of Figure 1. The predicted maximum pullup is 24.7 msec; the pullup measured from the finite-difference data of Figure 4.2 is 24 msec, so the agreement is excellent.

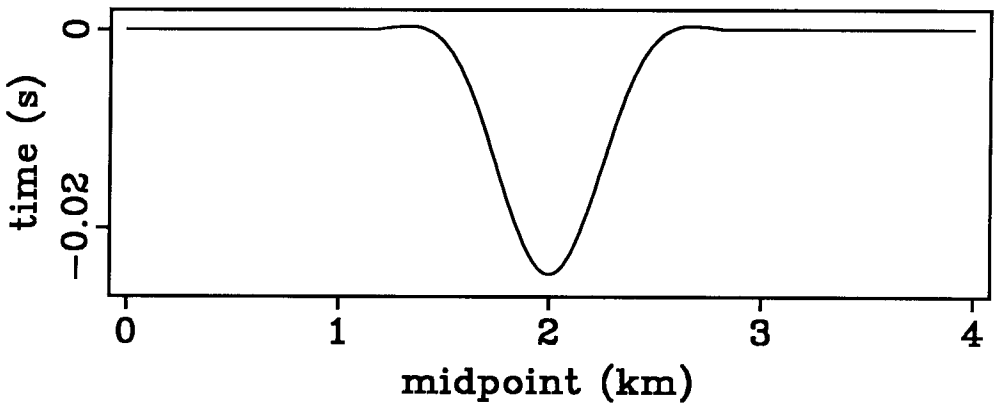

FIG. 4.35. Change in migrated traveltime τ for the data of Figure 4.2, predicted using the $\mathbf{G}_\tau$ operator. The peak pullup value is 24.7 msec.

The $\mathbf{G}_\tau$ operator can be inverted using SVD just as the $\mathbf{G}_s$ operator is. The result of performing such an inversion is shown in Figure 4.36. The lateral resolution is good, but the vertical resolution is far worse than that for the comparable $\mathbf{G}_s$ inversion in Figure 4.17. The singular spectrum for this $\mathbf{G}_\tau$ operator (Figure 4.37) decays even more rapidly than that for $\mathbf{G}_s$ (Figure 4.22); it is dominated by the first few large singular values. However, the dominant singular vectors are different for $\mathbf{G}_s$ and for $\mathbf{G}_\tau$. The first four such model-space singular vectors for $\mathbf{G}_\tau$ are shown in Figure 4.38. The $\mathbf{G}_s$ operator is insensitive to lateral wavelengths longer than the resonant wavelength. The $\mathbf{G}_\tau$ operator, on the other hand, is most sensitive to the longest wavelength components of the model. Unfortunately, because it is nearly a pure pullup, it is very insensitive to vertical changes, and so has poor vertical resolving ability.

Because the two operators are sensitive to different wavelength components of the model space, one could hope to improve resolution by joint inversion of the two operators. Such an inversion is shown in Figure 4.39. The horizontal resolution is better than for the $\mathbf{G}_s$ operator in Figure 4.17, and the vertical resolution is similar. The principal difference is that the positive sidelobes are lessened.

The use of mixed units creates a problem for the joint inversion. The $\mathbf{G}_s$ operator relates slownesses to slownesses, so it is itself dimensionless. The $\mathbf{G}_\tau$ operator relates slownesses to times, so it carries length. Thus, changing the units for measuring length can radically change the relative magnitudes of the two operators. To combine them, a weighting scheme is required to make them scale the same. In this example, the obvious length parameter for conversion is the depth of the reflector. For the inversion shown in Figure 4.39, the $\mathbf{G}_\tau$ operator is divided by the reflector depth, making it dimensionless like the $\mathbf{G}_s$ operator, before performing SVD on the combined matrix.

A more general approach to scaling operators with mixed units is to make all the parameters and operators dimensionless by using only relative changes. That is, instead of considering magnitudes of changes in interval slowness, Δm, migration slowness, Δs, migrated time, $\Delta \tau$, and midpoint, Δy, recast all the equations in terms of the normalized changes $\Delta m / m$, $\Delta s / s$, $\Delta \tau / \tau$, and $\Delta y / y$. Now all the variables are dimensionless, and scaling problems do not arise. For flat beds and a constant slowness background, one has $z_d = s\,\tau$, and it is easy to show that the weighting of $\mathbf{G}_\tau$ by z_d used above is equivalent to using normalized, dimensionless variables. In the more general case, the division by y might appear troublesome, because the location of the origin of the y axis coordinates is arbitrary. However, in

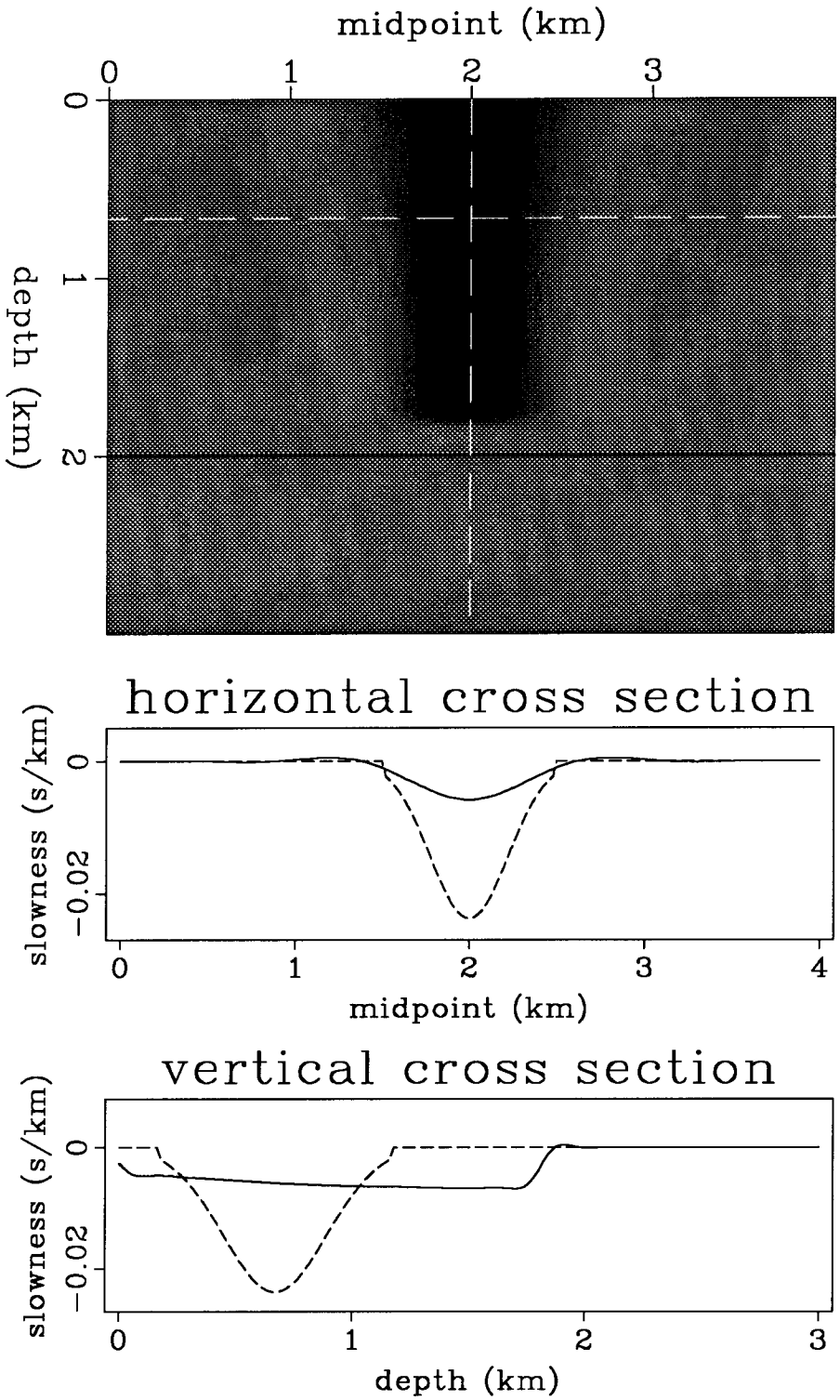

FIG. 4.36. Result of forward modeling and inverting the $\mathbf{G}_\tau$ operator. The anomaly model is that of Figure 4.4. The top picture shows the inverted anomalous interval slowness field. The lower figures show vertical and horizontal cross sections through the center of the Gaussian anomaly. Input values of the anomaly are shown as dashed lines for comparison.

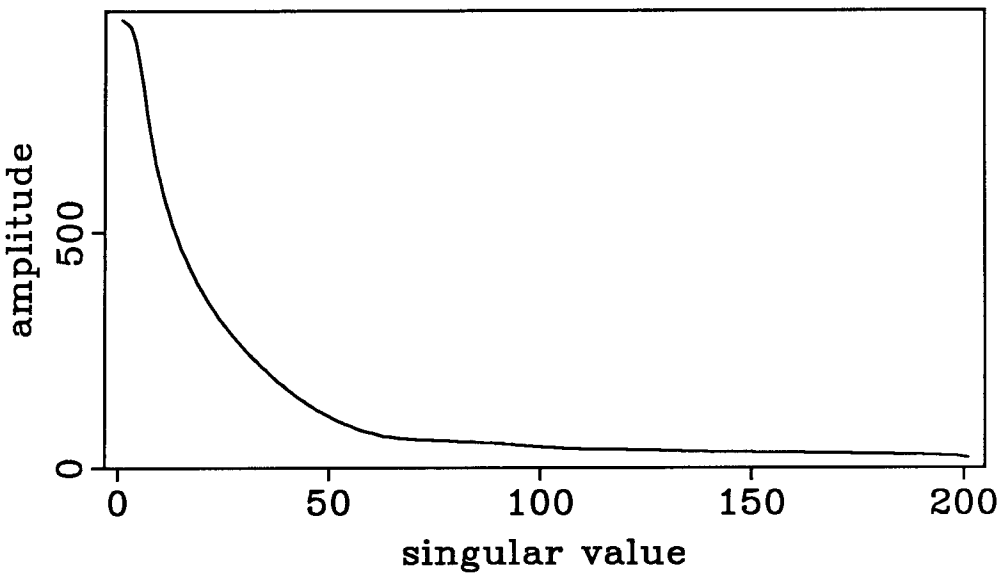

FIG. 4.37. Singular value spectrum for the $\mathbf{G}_\tau$ operator used in the inversion shown in Figure 4.36.

section 3.7 I showed that y and τ are not really independent variables, and so in principle one could suppress y altogether.

The inversion of G_τ and the joint inversion of $\mathbf{G}_s$ and $\mathbf{G}_\tau$ are more sensitive to singular value clipping or damping than are the rest of the inversions shown here. For most of the examples in this chapter, all non-zero singular values are inverted. Here the smallest singular values of G_τ are too small and must be clipped or damped to produce a reasonable result.

Fragmented reflectors

I have used continuous reflectors for all the inversion examples so far. In field data, reflector continuity can vary widely; often only portions of reflectors can be identified. Is the inversion degraded greatly if pieces of the reflectors are missing? To test this, I divided the dipping bed of Figure 4.4 first into segments with small gaps, and then into a few isolated pieces. Figure 4.40 shows the inversion of the first of these examples, using many short reflector segments. The inversion is noisier than that of Figure 4.21, which used a continuous reflector for the same inversion. Numerous artifacts are seen arising from the truncated edges of the bed segments, but the anomaly reconstruction is not degraded unreasonably. Figure 4.41 shows the second example, using four long pieces with wide gaps. Now the reconstruction is much worse. Too much of the bed is missing to illuminate the anomaly adequately,

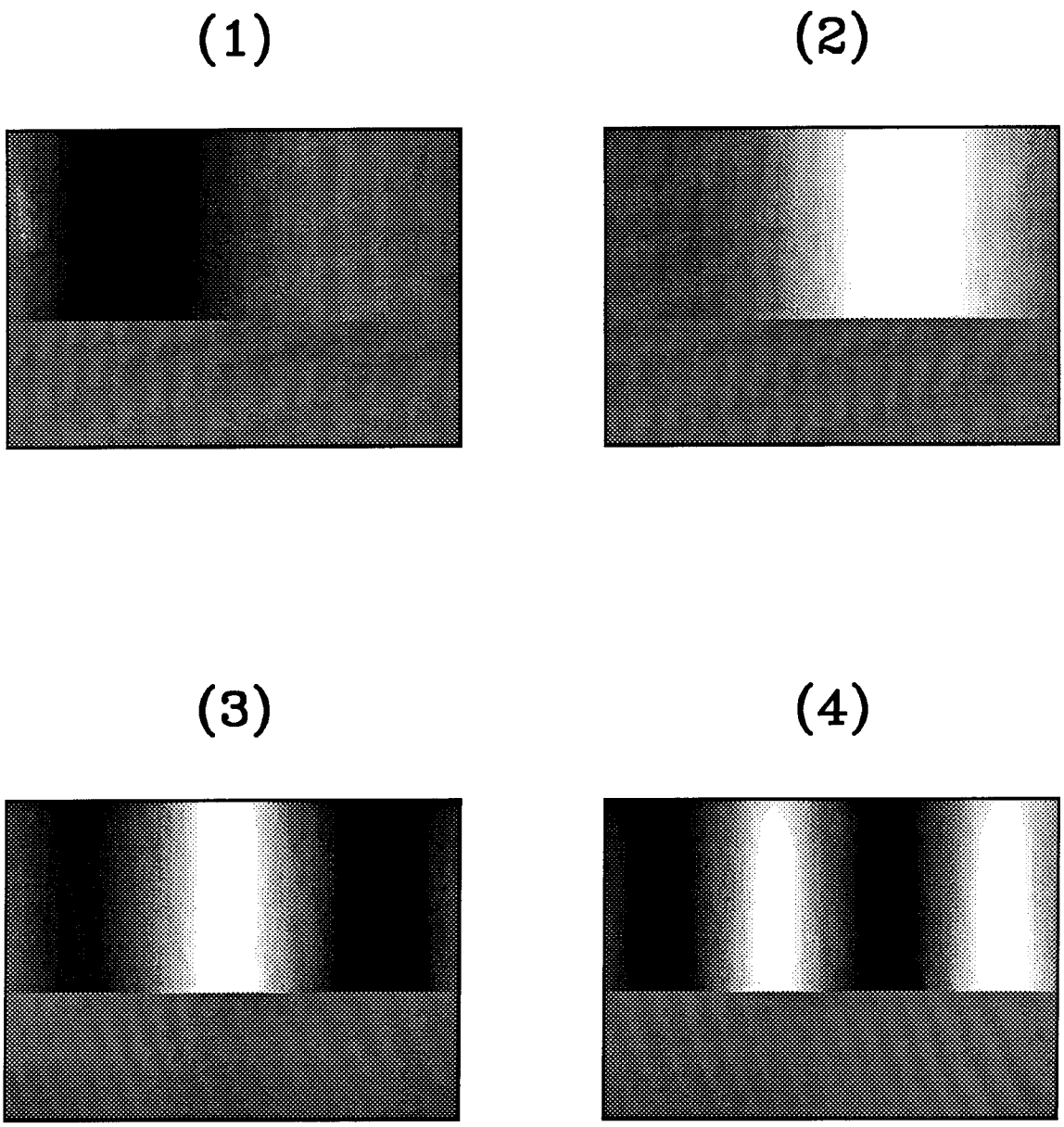

FIG. 4.38. The first four model-space singular vectors for the $\mathbf{G}_\tau$ operator used in the inversion shown in Figure 4.36. The singular vector numbers correspond to the singular values in Figure 4.37. The axes of the plots are the same as for the model in Figure 4.4 and the inversion in Figure 4.36.

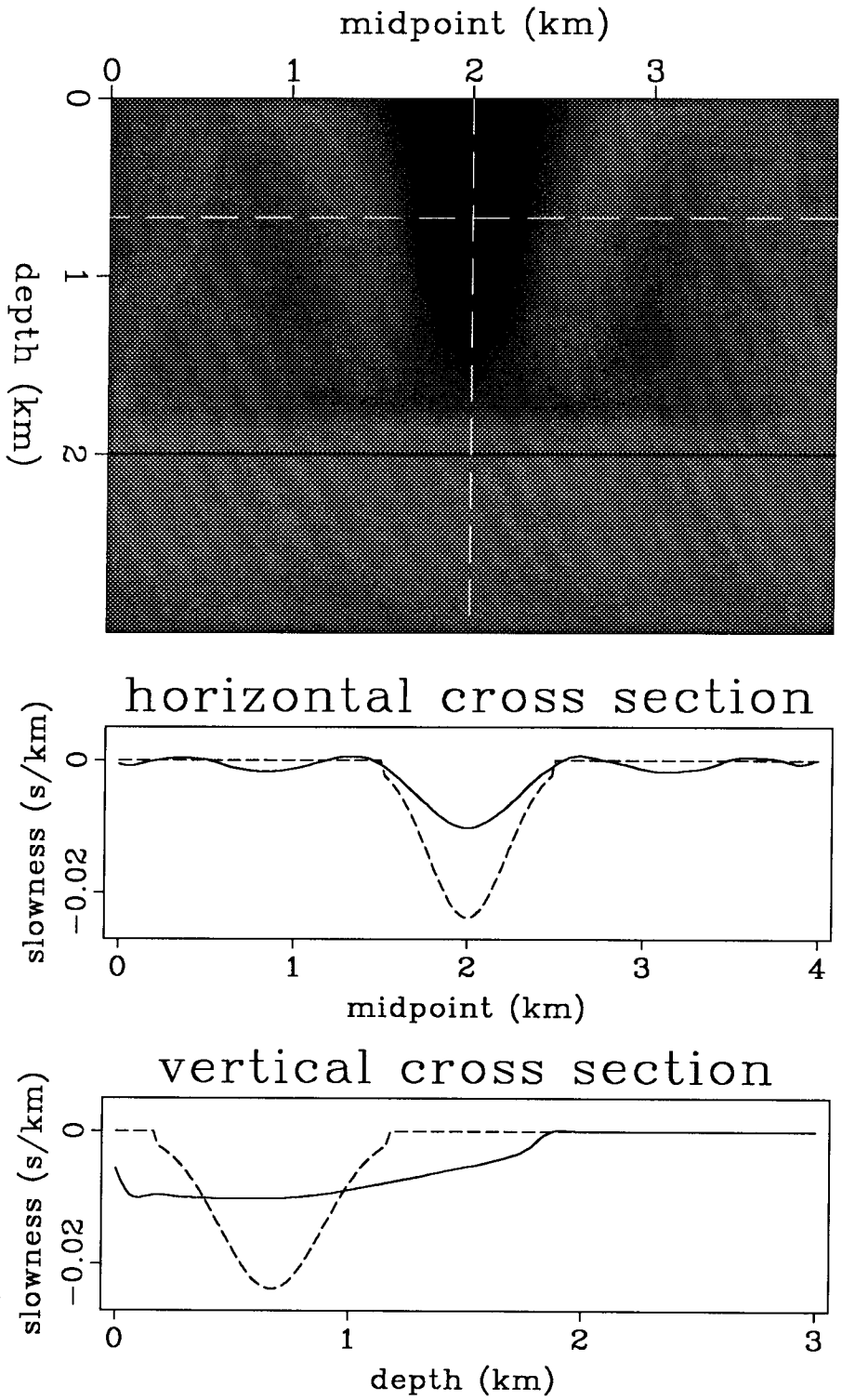

FIG. 4.39. Result of forward modeling and jointly inverting the $\mathbf{G}_s$ and $\mathbf{G}_\tau$ operators. The anomaly model is that of Figure 4.4. The top picture shows the inverted anomalous interval slowness field. The lower figures show vertical and horizontal cross sections through the center of the Gaussian anomaly. Input values of the anomaly are shown as dashed lines for comparison.

and the edge artifacts dominate. In principle, these edge artifacts could be lessened by treating the edges as point diffractors made up of all dips, and using at those points a $\mathbf{G}_s$ operator that contains a wide range of dips. I have not attempted this experiment yet.

4.5 FORMULATING NONLINEAR INVERSION

So far I have discussed the inversion of the linear operator relating perturbations in interval and migration slownesses. This linear inversion is likely to be inadequate for finding interval slownesses for realistic seismic data, because the problem of inverting migration slownesses for interval slownesses is in general significantly nonlinear. However, the linear operator presented here can be used to provide a gradient direction to guide an iterative, nonlinear inversion. The basic idea of any such inversion scheme is to begin with an initial model of interval slownesses and then update it until the corresponding migration slownesses better match those measured from the data.

Perhaps the simplest approach would be to pick migration slownesses using the methods of chapter 2, in the same fashion that conventional stacking velocities are picked. The interval slowness model could then be updated iteratively to minimize the least-squares error between the predicted slownesses and the picked values. I believe, however, that this would be a poor approach. Stacking or migration slownesses average the effects of interval slownesses and so are insensitive to small changes in interval slownesses. The corollary to this, however, is that the inversion of migration slownesses for interval slownesses can be unstable; small picking errors can get amplified into large errors in interval slowness. This instability is a familiar problem with conventional inversion of stacking velocities using the Dix rms approximation.

As discussed briefly in chapter 2, conventional velocity analysis involves picking peak values that maximize some measure of the quality of the corresponding imaged section. The total semblance or energy in the imaged section thus can be used as an objective function measuring the optimality of the velocity function. The goal of an optimization algorithm is then to maximize this objective function; this still corresponds to finding the peaks that one would conventionally pick, but the penalty for deviating from the peaks is determined by the contours of the energy or semblance function, not by the quadratic penalty function implicit in least-squares fitting of picked peaks.

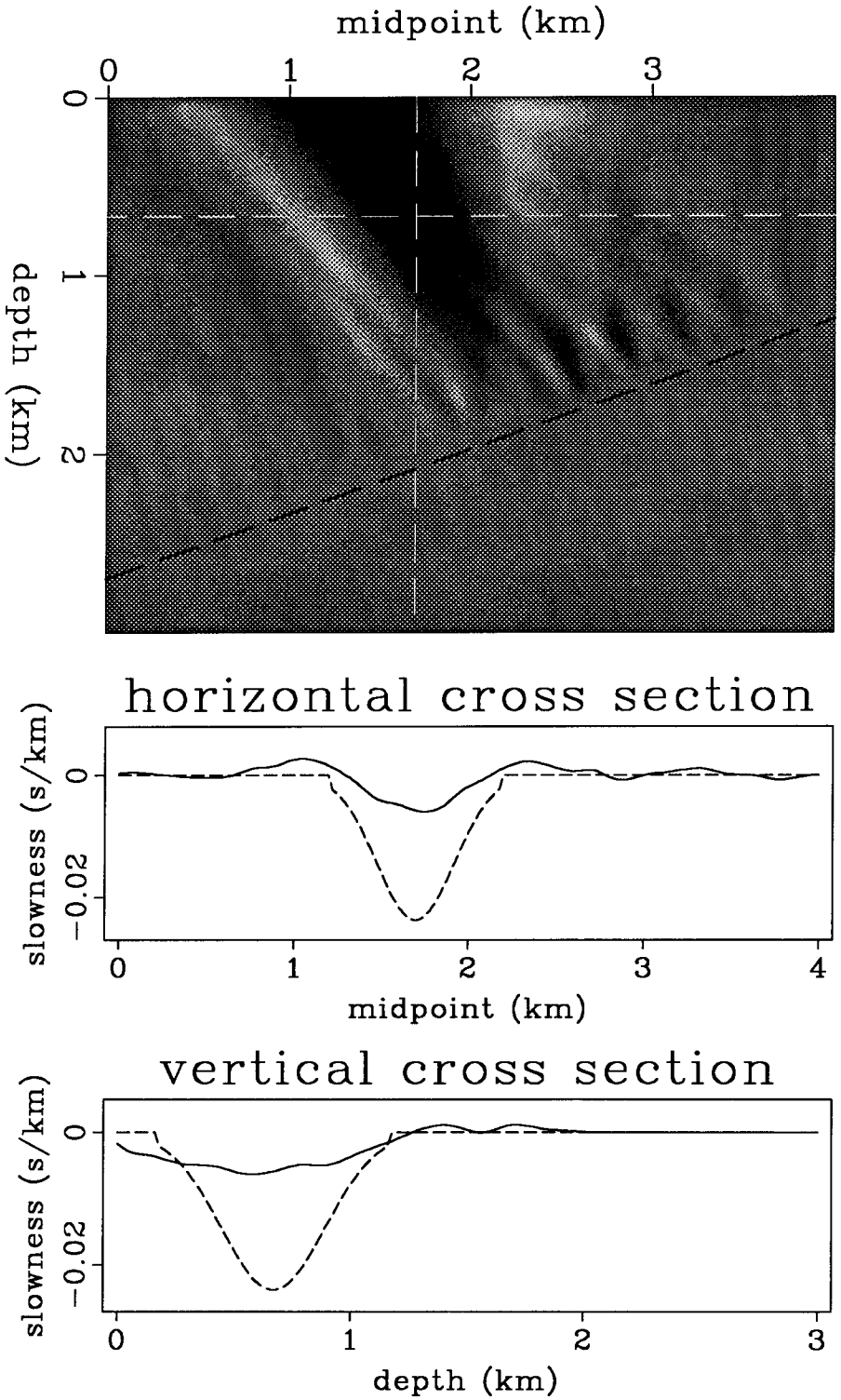

FIG. 4.40. Result of forward modeling and inverting the $\mathbf{G}_s$ operator for a perforated, dipping bed. The anomaly model is that of Figure 4.4. The top picture shows the inverted anomalous interval slowness field. The lower figures show vertical and horizontal cross sections through the center of the Gaussian anomaly. Input values of the anomaly are shown as dashed lines for comparison.

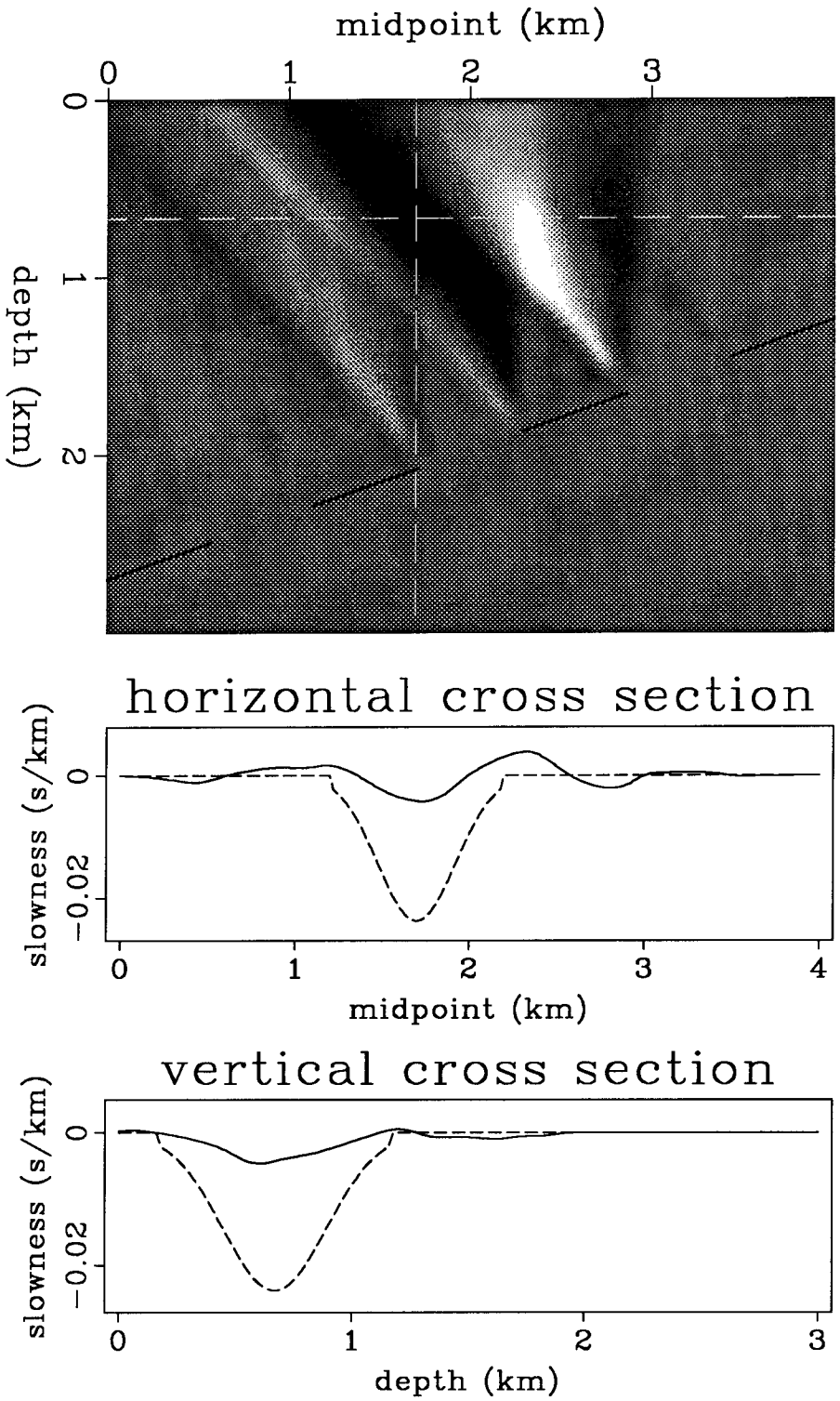

FIG. 4.41. Result of forward modeling and inverting the $\mathbf{G}_s$ operator for a severely fragmented, dipping bed. The anomaly model is that of Figure 4.4. The top picture shows the inverted anomalous interval slowness field. The lower figures show vertical and horizontal cross sections through the center of the Gaussian anomaly. Input values of the anomaly are shown as dashed lines for comparison.

Casting velocity analysis as an optimization algorithm in this way is not new to this dissertation. The method has been developed extensively by Toldi (1985), and the approach presented here is explicitly based on that work. The principle difference here is that the incorporation of dip using migration velocities in place of stacking velocities introduces several complications not present in Toldi's work. I focus here on those differences, and refer the reader to Toldi (1985) for further discussion of the implementation of such algorithms.

The basic data used for the inversion is a cube of migration slownesses, generated as described in chapter 2, by imaging with a suite of constant slowness functions. The data is a function of the three parameters midpoint y, migrated time τ, and migration slowness s. For an objective function, I use the total energy E, (smoothed over an appropriate window), so the data cube can be converted to an energy cube $E(s,y,\tau)$. Specifying a slowness function $\mathbf{s}$ defines a particular relation $s(y,\tau)$. The objective function $Q(\mathbf{s})$ is then defined as the total energy in the section,

$$Q(\mathbf{s}) \equiv \sum_{\mathbf{d}} E(s_d(y_d,\tau_d),y_d,\tau_d) . \tag{4.3}$$

The optimization algorithm uses a gradient to update iteratively a starting model. The gradient $\nabla_{\mathbf{s}} Q$ of the objective function Q with respect to the migration slownesses $\mathbf{s}$ can be evaluated easily from the energy cube. What is really needed for a good algorithm, however, is the gradient $\nabla_{\mathbf{m}} Q$ of the objective function Q with respect to changes in an underlying model $\mathbf{m}$ of interval slowness as a function of the physical location x and depth z. To derive this one can use the linear operator $\mathbf{G}$ derived in chapter 3 to specify a relation between $\mathbf{s}$ and $\mathbf{m}$.

Start with an interval velocity model $\mathbf{m}(x_a,z_a)$. Suppose also that a set of reflecting points $\mathbf{d}=(x_d,z_d)$ is given, and that the migration slownesses $s_d \equiv s(\mathbf{d})$ are known. A map between the reflecting points $\mathbf{d}$ and the corresponding data points (y_d,τ_d) is also needed. Thus all three variables s_d, y_d, and τ_d are specified as functions of the reflector point coordinates x_d and z_d and of the interval slowness model $\mathbf{m}$, and all will change as $\mathbf{m}$ is changed. The objective function Q can then be redefined as a function of the interval slowness model $\mathbf{m}$

$$Q(\mathbf{m}) \equiv \sum_{\mathbf{d}} E\left[s_d(\mathbf{m}),\tau_d(\mathbf{m}),y_d(\mathbf{m})\right] . \tag{4.4}$$

An application of the chain rule yields

$$(\nabla_{\mathbf{m}}\mathbf{Q})_a = \frac{\partial Q}{\partial m_a} = \sum_{\mathbf{d}} \left[\frac{\partial E}{\partial s_d}\frac{\partial s_d}{\partial m_a} + \frac{\partial E}{\partial \tau_d}\frac{\partial \tau_d}{\partial m_a} + \frac{\partial E}{\partial y_d}\frac{\partial y_d}{\partial m_a} \right] . \tag{4.5}$$

In computing this gradient, the partial derivatives of E with respect to s_d, τ_d, and y_d can be computed by finite difference approximations applied to the energy data cube. For example,

$$\frac{\partial E}{\partial s_d} \approx \frac{E(s_d+\Delta s_d, y_d, \tau_d) - E(s_d, y_d, \tau_d)}{\Delta s_d} \tag{4.6}$$

and similarly for y_d and τ_d. The remaining derivatives in equation 4.5 are just the terms of the **G** operator from chapter 3: $\partial s_d / \partial m_a = \mathbf{G}_s(\mathbf{d},\mathbf{a})$, etc. Thus equation (4.5) can be written more compactly as

$$\nabla_{\mathbf{m}} Q = \mathbf{G}_s^T \nabla_{\mathbf{s}} Q + \mathbf{G}_y^T \nabla_{\mathbf{y}} Q + \mathbf{G}_y^T \nabla_{\tau} Q \tag{4.7}$$

where the superscript T denotes the matrix transpose.

A simple iterative optimization algorithm that uses this gradient to define a steepest ascent direction can be outlined as follows:

Set initial interval slowness model **m**
Set initial values of $\mathbf{s}_d$, τ_d, and $\mathbf{y}_d$
Calculate initial dip spectrum estimate $\boldsymbol{\theta}_d$ from time dips and $\mathbf{s}_d$
Compute **G**(**d**,**a**) from initial **m** and $\boldsymbol{\theta}_d$

Repeat until ΔQ is small enough
{
1. Compute $\nabla_{\mathbf{s}} Q$, $\nabla_{\tau} Q$, and $\nabla_{\mathbf{y}} Q$ by finite differences
2. Form $\nabla_{\mathbf{m}} Q$ at the current model **m**:
$$\nabla_{\mathbf{m}} Q = \mathbf{G}_s^T \nabla_{\mathbf{s}} Q + \mathbf{G}_y^T \nabla_{\mathbf{y}} Q + \mathbf{G}_y^T \nabla_{\tau} Q$$
3. Line search for α that maximizes $Q(\mathbf{m}+\alpha\nabla_{\mathbf{m}} Q)$
4. Update model
$$\Delta\mathbf{m} = \alpha\nabla_{\mathbf{m}} Q$$
$$\mathbf{m} = \mathbf{m} + \Delta\mathbf{m}$$
$$\mathbf{s}_d = \mathbf{s}_d + \mathbf{G}_s\Delta\mathbf{m}$$
$$\tau_d = \tau_d + \mathbf{G}_{\tau}\Delta\mathbf{m}$$
$$\mathbf{y}_d = \mathbf{y}_d + \mathbf{G}_y\Delta\mathbf{m}$$
4. Update $\boldsymbol{\theta}_d$ using new $\mathbf{s}_d$
5. Compute **G**(**d**,**a**) for new **m** and $\boldsymbol{\theta}_d$
}

Many details of this algorithm deserve further explanation. The initial information needed to start the iterations consists of more than just a beginning model of interval slownesses. One also needs a corresponding model of migration slownesses, and a map relating subsurface points (x_d, z_d) to their images in the data (y_d, τ_d). The starting estimate of migration slownesses is important, because errors in the initial relation between interval and migration slownesses will propagate through further iterations. The starting values of migration slowness will be equal to the interval slowness for a constant slowness model, and the map between (x_d, z_d) and (y_d, τ_d) will be trivial. For more complicated starting models, these relations can probably be calculated best by using ray-traced traveltimes. One also needs an initial estimate of dip spectra at each point **d**. This can be estimated from the time dips $d\tau/dy$ measurable in the migrated data using the relation

$$\tan\theta = \frac{1}{2s}\,\frac{d\tau}{dy}\,. \tag{4.8}$$

This conversion of time dips to physical dips depends on the current estimate of the migration slowness s, and so it must be updated at each iteration. The line search of step 3 is needed because this is a nonlinear problem; the gradient tells the direction in which to change the model, but not how far to proceed in that direction. During the search one will need to compute several values of $\Delta\mathbf{m}$, $\Delta\mathbf{s_d}$, $\Delta\mathbf{y_d}$, and $\Delta\boldsymbol{\tau}_\mathbf{d}$. New values of y_d and τ_d will generally not lie on grid points, and will have to be interpolated. Similarly, values of θ_d will need to be interpolated.

The need to interpolate values of y_d, τ_d, and especially, θ_d, implies that this formulation of the algorithm will work best if a dense mesh of reflecting points **d** is used. The size of the **G** matrices and the cost of computing them increases directly with the number of reflecting points used. If the **G** operators become too large to store on disk and instead need to be recomputed at each use, the computational penalty could be excessive, because of the repeated use of **G** during the line search in step 3. It would be attractive to be able to use only the parts of the data that correspond to strong, well defined reflectors, thus cutting down on the number of reflecting points considered. However, only the (y_d, τ_d) coordinates of these reflectors will be known at the start, not the (x_d, z_d) values of the physical reflector location, so if one fixes the set of points (x_d, z_d) to be used, their image points (y_d, τ_d) may wander away from the strong reflectors. Moreover, interpolating dip values θ_d may lead to inaccuracies, because dips can change abruptly. For these reasons, it might prove better to compute gradients with respect to a fixed grid of (y_d, τ_d) coordinates, not with respect to a fixed set of (x_d, z_d) points as assumed in the algorithm outlined

above. This type of approach is also possible, but introduces its own further set of complications. I discuss in Appendix E an alternative algorithm based on using a fixed (y_d, τ_d) grid.

Both the algorithm given here and that outlined in Appendix E assume that the mapping between (x_d, z_d) and (y_d, τ_d) is updated using the computed changes Δy_d and $\Delta \tau_d$. This updating can also be done by explicit ray tracing through the new slowness model, and such a ray tracing approach may prove more robust. Both of the algorithms can also be modified readily to use DMO-corrected stacking slownesses instead of migration slownesses. The only real change is in the use of unmigrated positions in place of migrated ones.

Whichever approach is chosen, a practical implementation probably would not use the simple steepest ascent method described above. Conjugate gradient methods use the gradient information in more sophisticated ways to accelerate convergence greatly. Such techniques are described in detail in Luenberger (1983), Press, et al. (1986), and Gill et al. (1981). Toldi (1985) discusses the use of data space smoothing to enhance convergence of early iterations if a poor starting model is used. He also examines incorporation of constraints during the optimization. Only the long wavelength components of the model can be expected to be resolved well, so constraints can be included that bias the optimization against short wavelength features. One simple way to incorporate such smoothness constraints is to add penalty terms to the objective function Q, for example,

$$Q(\mathbf{m}) \equiv \sum_{\mathbf{d}} E\left[s_d(\mathbf{m}), \tau_d(\mathbf{m}), y_d(\mathbf{m})\right] - \mathbf{m}^{\mathbf{T}}(\beta \mathbf{D}_{\mathbf{x}}^{\mathbf{T}}\mathbf{D}_{\mathbf{x}} + \epsilon \mathbf{D}_{\mathbf{z}}^{\mathbf{T}}\mathbf{D}_{\mathbf{z}})\mathbf{m} \qquad (4.9)$$

where $\mathbf{D}$ is a derivative matrix and β and ϵ are adjustable damping parameters determining the degree of lateral and vertical smoothing to be used. Other constraints based on well-log data, existing geological models, or other a priori information could be included similarly. For further discussion of how to include such constraints in optimization problems, see Claerbout (1976) or Menke (1984).

DISCUSSION AND CONCLUSIONS

In this chapter I have examined modeling of a canonical velocity anomaly, a circular, Gaussian tapered blob against a constant background, using the **G** operator of chapter 3 for both flat and dipping beds. I also considered inversion of this linear operator using singular value decomposition to look at the resolution possible. The modeling results show a general agreement with anomalous slowness values measured from finite-difference synthetic data. These results also suggest that the major limitation to measuring migration slowness anomalies lies in trying to compensate for the rapid movement of events between panels migrated with different slownesses. It is easier to measure slowness anomalies if all migration is done at a single background slowness, or if unmigrated, DMO-corrected slownesses are used instead.

Because measuring slowness by summing wavelets can give a different estimate of optimal moveout curvature than that predicted by least-squares fitting of traveltimes, further modeling should be done to quantify these systematic deviations, and to see if they can be compensated for. This modeling should probably be done using ray tracing; finite-differencing is computationally slow and introduces artifacts that can bias velocity analyses.

The resolution studies in this chapter show that inverting migration slownesses is not as accurate as an ideal traveltime tomographic inversion, but the result can be close. The principle limitation is that the singular value spectrum is dominated by a few principal resonances. These resonances cause sidelobes to form during inversion. These sidelobes can be lessened by joint inversion of sections of the acquisition aperture, or by having enough reflectors present in the data.

Velocity analysis using either DMO or prestack time migration uses traveltimes for common reflection point gathers. The transformation from common midpoint to common reflection point eliminates the principal cause of multiple values in velocity spectra. Both methods are based on estimating moveout in CRP gathers; the difference lies in whether the velocity information is measured at migrated or at unmigrated locations. Prestack migration moves events in both offset and midpoint. This movement can be decoupled into a summation over a generalized moveout trajectory, followed by a zero-offset migration. Both stages contain velocity information. The preliminary results here suggest that the latter migration stage, although extremely useful for interactive analysis, as shown in chapter 2, can cause problems for automatic velocity analysis methods based on maximizing the energy or coherence over offset along the moveout trajectory. Dmo-corrected velocities are effectively equivalent to the result of backing out the zero-offset migration stage from prestack

time-migration velocities, and appear to be easier to measure reliably. The linear operator derived in chapter 3 can be used in either case, and the resolution studies in this chapter apply to inversion of DMO velocities as well as migration velocities.

For migration velocity analysis here I use data that is prestack migrated at various velocities, with stacking an implicit part of the migration. A closely related approach would be to migrate all offsets using a single reference velocity model, and attempt to estimate the residual traveltime differences remaining between different offsets. In effect, this would be another way to estimate the differences between the predicted and actual moveouts in CRP gathers. If the background velocity is constant, or only gradually varying, I see no intrinsic advantage to this alternate approach. The possible advantage arises if one uses depth migration instead of time migration for the background. It might then be possible to obtain better resolution, since one more directly compensates for variations in the background; computing only a residual moveout this way links imaging and velocity analysis more closely. This is the gist of the approach suggested by Al-Yahya (1987) and extended by Etgen (1988).

In principal, it should be possible to obtain similar results with the techniques of this thesis by combining them with a layer stripping approach. One could compute the velocities for the shallow depths, downward continue the data using these computed velocities, and then compute velocities for the deeper regions using the downward continued data. In the second stage one would, in effect, be computing only a residual moveout for the CRP's, since the effects of the upper layers would be removed. It remains to be seen what method, or combination of methods, will prove most useful in practice.